The Dissertation Committee for Shravanthi Reddy certifies that this is the approved version of the following dissertation:

Fluid and Solid Mechanics in the Step and Flash Imprint Lithography Process

Committee:

_____
Roger T. Bonnecaze, Supervisor

_____
John G. Ekerdt

_____
S.V. Sreenivasan

_____
Kamy Sepehrnoori

_____
Venkat Ganesan

Fluid and Solid Mechanics in the Step and Flash Imprint Lithography Process

by

Shravanthi Reddy, B.S.E., M.S.E.

Dissertation

Presented to the Faculty of the Graduate School of

The University of Texas at Austin

in Partial Fulfillment

of the Requirements

for the Degree of

Doctorate of Philosophy

The University of Texas at Austin

May 2006

To my parents.

Acknowledgments

This dissertation and the years of study that accompany it have been an absolute pleasure for me because of the people involved, and I only regret that it has to end! First and foremost I am extremely grateful to my Ph.D. advisor Roger Bonnecaze. His enthusiasm, patience, and gifted teaching ability have made this experience consistently enjoyable, and he has given me a perfect example of how to be a good researcher as well as a great teacher and colleague. I also feel very lucky to have worked with Randy Schunk at Sandia National Laboratories, whose excitement for our work was inspiring; he taught me how to see and solve problems in a unique and practical way. Thanks to my committee member Kamy Sepehrnoori for always being available to talk about my work and help me brainstorm when the code wasn't working, his suggestions have been extremely valuable and his friendship even more so. I am appreciative of Buddie Mullins' frequent talks and concern for all things academic or tennis related; I have relied on his friendship and guidance.

On a personal level, I am unable to express how grateful I am to my parents Ramakrishna and Prasanna Reddy for their constant support and encouragement. They have gone to so many lengths to give me the best education and life experience possible, and I am amazed by their own life stories and constantly inspired to be the best I can be in their honor and example. My sister, Anj, has also been a great example to me, and I thank her for always checking up on me and being a good listener. My brother, Vik, and I share many qualities, and I am grateful for his support. I was very lucky to enter UT with classmates so full of energy and to have made friends who have made all five years

of this experience so memorable. Whether studying for our qualifying exams or celebrating the passing of preliminary exams or watching UT win the National Championship, we have made our graduate experience truly remarkable. My experiences in Albuquerque and Austin would not have been the same without the many friends I have made outside of my program; I am grateful they came into my life and made my time in these places so enjoyable.

Fluid and Solid Mechanics in the Step and Flash Imprint Lithography Process

Shravanthi Reddy, Ph.D.

The University of Texas at Austin, 2006

Supervisor: Roger T. Bonnecaze

Step and Flash Imprint Lithography (SFIL) has become a promising technology to bring integrated circuit feature sizes to the nanometer scale. It is a molding process in which liquid monomer is imprinted by a patterned template, with a UV cure to polymerize the monomer into its patterned form. The success of the process depends heavily on fluid management issues presented in this study. Important insights are obtained by detailed analysis of the physics of the fluid and solid mechanics, making it possible to manipulate issues including imprint time and pressure, template deformation, and feature filling in order to drive the process to becoming a successful and efficient manufacturing technique.

The fluid mechanics are simulated using lubrication theory. The solid mechanics governing elastic deformation of the template are simulated using thin plate theory. The solution of this coupled fluid-solid mechanics problem provides a dynamic simulation of the elastic deformation of the template and the time evolution of the fluid flow and pressure. The interplay of elastic, viscous, and capillary forces govern the behavior of the fluid and solid mechanics. In order to avoid extreme viscous or capillary pressures that lead to elastic deformation, it is found that an exact balance of the viscous and

capillary forces throughout the imprint yields negligible deformation. The imprint time can be reduced using multiple drops and apportioning drop volume appropriately.

A study of feature filling in both the lateral and vertical directions is presented, and it is found that the aspect ratio and geometry of the feature determine its ability to fill. A vertical study of the fluid-air interface as it moves into a template feature provides new understanding of the mechanics of contact line motion and interface reconfiguration. A modified pressure boundary condition in the lubrication code handles fluid motion through template features in the lateral direction. Both studies determined that high aspect ratio features are more difficult to fill, either trapping air due to interface stretching or requiring a lag time before fluid moves into the feature. This study provides a better understanding of these fluid issues and presents insights into the details of the process that can be controlled to make the process a viable technology in the future of imprint lithography.

Table of Contents

List of Figures

Chapter 1: Introduction

1.1. Historical Context of Electronics

Exactly one century ago, the 1906 Nobel Prize for Physics was awarded to Joseph John Thompson of the University of Cambridge for his experiments proving the existence of the electron [1]. Even before Thompson's experiments brought a fundamental understanding of the nature of electrons, the concept of a charged particle responsible for electric phenomena had been postulated by Benjamin Franklin, whose famous kite experiments in 1752 showed lightning to be a form of electrical discharge. Other scientists had experimented with electricity before Franklin, including the English physicist Stephen Gray and the German physicist Otto von Guericke. In ancient Greece, Thales observed that an electric charge could be generated by rubbing amber, for which the Greek word is electron.

In the same year as Thompson won his Nobel Prize, an American inventor and physicist Lee De Forest created the vacuum tube triode, or audion as he called it, which allowed current to flow between two wires in an evacuated tube by controlling the current delivered from a third wire, shown in Figure 1.1. Although vacuum tube diodes had been
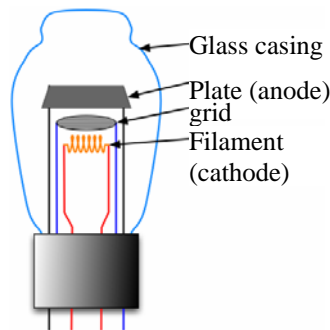
Figure 1.1: The vacuum tube triode. Most evacuated tube diodes and triodes were encased in glass, although any insulating material would work.

made even in the late 1800's by several scientists including Thomas Edison, this was the first device in which the current direction could be controlled. This development, along with the fundamental understanding of electricity that Thompson made possible through his discovery of the electron, paved the way for scientists to begin manipulating electricity at will. The motivation for the development of the triode was initially the need for amplification of audio signals to make A.M. radio possible. The vacuum tube triode's use for other electronic devices quickly became apparent and was intrinsic to the development of the first computers.

1.2. From Vacuum Tubes to Solid State Transistors

Vacuum tubes were used in several different computer designs in the late 1940s and early 1950s. But the limits of these tubes were soon reached. As the electric circuits became more complicated, one needed more and more triodes, *i.e.* many more tubes, so that computers were built with as many as 10,000 vacuum tubes and occupied over 93 square meters of space; one of the first computers, ENIAC (Electronic Numerical Integrator and Computer) weighed 30 tons. The tubes tended to leak, and the metal that emitted electrons in the vacuum tubes burned out – ENIAC needed 2,000 tubes replaced every month. The tubes also required so much power that big and complicated circuits were too large and took too much energy to run.

The problems with vacuum tubes led scientists and engineers to think of other ways to make three terminal devices. Instead of using electrons in a vacuum, scientists began to consider how one might control electrons in solid materials, like metals and semiconductors. Already in the 1920s, scientists understood how to make a two terminal
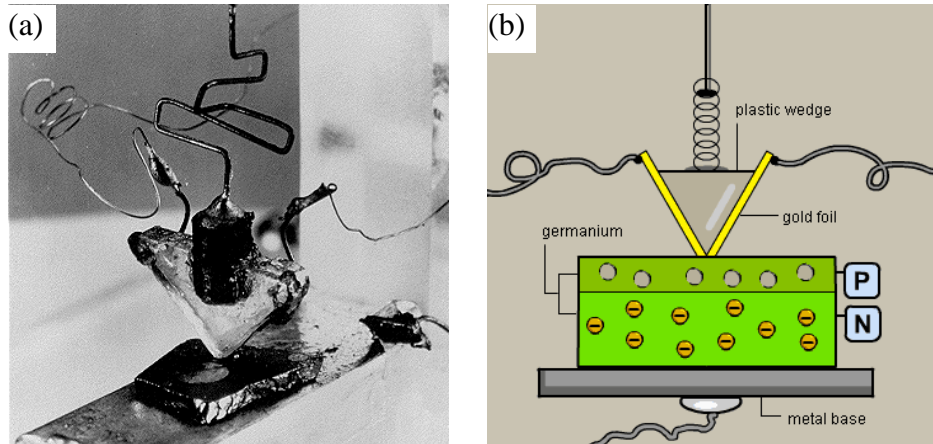
Figure 1.2: The first point contact transistor. (a) The transistor made by Bardeen and Brattain, which operated as a speech amplifier, 1947; (b) A schematic of a germanium semiconductor with p-type and n-type doping for voltage amplification and gold foil acting as the charge carrier.

device by making a point contact between a sharp metal tip and a piece of semiconductor crystal. These point-contact diodes were used to rectify signals (change oscillating signals to steady signals), and make simple A.M. radio receivers (crystal radios); however, it took many years before the three terminal solid state device - the transistor - was discovered.

In 1947, John Bardeen and Walter Brattain, employees of Bell Telephone Laboratories, were trying to understand the nature of the electrons at the interface between a metal and a semiconductor. They realized that by making two point contacts very close to one another, they could make a three terminal device - the first "point contact" transistor, shown in Figure 1.2.

They quickly made a few of these transistors and connected them with some other components to make an audio amplifier. This audio amplifier was shown to chief executives at Bell Telephone Company, who were very impressed that it didn't need time to "warm up" (like the heaters in vacuum tube circuits). They immediately realized the
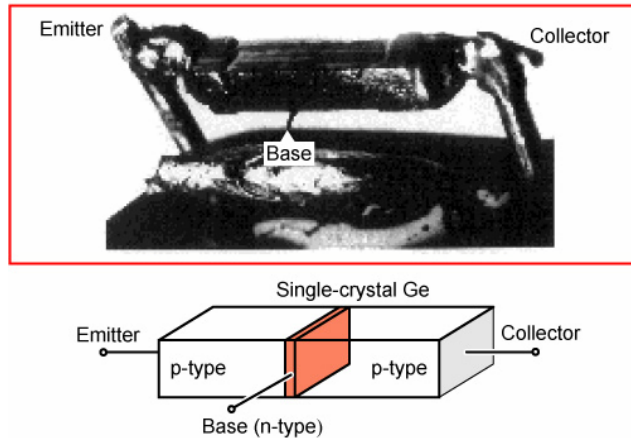
Figure 1.3: The first junction transistor by William Shockley; the emitter and collector are connected to semiconductor diffused with p-type dopant, forming a junction with a base that is connected to an n-type doped region in the center.

power of this new technology.

This invention was the spark that ignited a huge research effort in solid state electronics. Just 50 years after the Nobel Prize was awarded to Thompson for his proof of the existence of electrons, Bardeen and Brattain received the 1956 Nobel Prize in Physics, together with William Shockley, "for their researches on semiconductors and their discovery of the transistor effect," essentially for harnessing the electron flow in solid materials by making the material selectively conductive to carry charge in the region they chose. Shockley had developed a so-called junction transistor, shown in Figure 1.3, which was built on thin slices of different types of semiconductor material pressed together. The junction transistor could be manufactured more reliably, and its basic form is the same 50 years later.

1.3. Integrated Circuits and the New Era of Electronics

Transistors were initially made as individual components, working in concert with other components such as resistors and capacitors that were all mounted onto a board to create an electric circuit. Since they were much smaller than the vacuum tube triodes, many more could be used to make much more complex circuits, switching faster than the vacuum tubes and consuming much less power. With the ability to use more components, however, the electric circuits became more complex and the large number of separate components became unmanageable. In fact, the distances the electric signals had to travel between the components caused noticeable time delays. The process of connecting all the components was extremely labor-intensive, with each connection needing to be soldered by hand; if any of the connections were inadequate, the current would of course stop, and the broken connection would have to be found and fixed.

A new design for the circuit that would allow the components to pack closer together with easier assembly methods became necessary. Though the scientific revolution had made solid state transistors possible, an engineering revolution was required to fabricate whole circuits on a large scale. In 1958, Jack Kilby at Texas Instruments and Robert Noyce at Fairchild Camera (later to become co-founder of Intel) independently came up with ways to put transistors on the same piece of metal as other electrical components such as diodes, resistors and capacitors. This device became known as the integrated circuit, and it revolutionized the way electronics were made and the complexity of functions that could be combined into a single circuit.
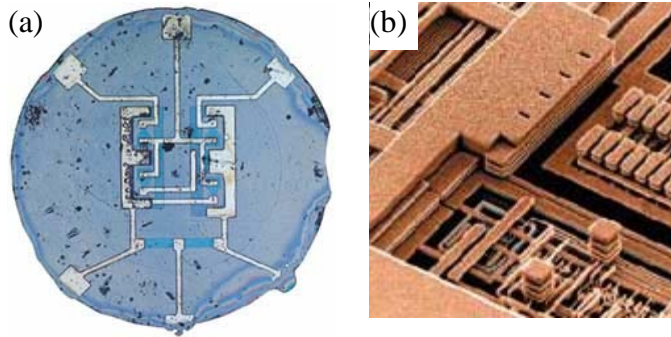
Figure 1.4: (a) Noyce's design of the first commercial integrated circuit, fabricated using an oxidation-diffusion process on a planar semiconducting substrate; (b) A modern integrated circuit by IBM. Copper is used for the metallic lines to enable high-speed operation; lines are as narrow as 0.13 microns.

Kilby won the Nobel Prize in Physics for the invention of the integrated circuit (the prize was awarded after Noyce had passed away, and since Nobel Prizes are not awarded posthumously Noyce could only be informally honored by Kilby's invitation of Gordon Moore, Noyce's co-founder of Intel, to the ceremony). Noyce was, however, more prescient in his chosen method for fabricating this so called "integrated circuit". He used a planar semiconducting substrate with oxidation and diffusion processes to create the circuits and used evaporated metal to form the connections between circuits. This planar process became the only efficient way to fabricate these circuits on a commercial scale; his design for the first commercially available integrated circuit is shown in Figure 1.4. Thus the invention of the integrated circuits heralded the era of modern electronics.

Noyce's introduction of oxidation and diffusion processes along with a planar fabrication process brought the manufacturing goal to realization. Through a series of manufacturing steps, a semiconductor in wafer form could be layered with oxide and selective regions could then be diffused with doping materials to make the semiconductor

selectively conductive or insulating, creating individual components (transistors, capacitors, etc.) on the same chip but yet isolated from one another except where metal interconnects were deposited using the evaporated metal source. This method of fabricating integrated circuits removed the human, labor-intensive component, which was time-consuming and low-yield, and made affordable large scale production possible. The method used by the electronics industry today has changed little since it was introduced, and the real revolutions in the industry during this time have come not in fundamental circuitry but in process modification, with a continuous push to make the process, known today as "microlighography", higher yield with higher resolution circuitry.

1.4. Microlithography

Soon after the first integrated circuits were made, a method was needed to commercialize and scale up the fabrication. The logical process was to make one mask that had the pattern for the integrated circuit on it, and then do as many pattern transfers as needed to reproduce that pattern in the silicon wafers. The premise of lithography in the electronics industry is akin to that of traditional lithography for reproducing artwork and patterns and has been in place for hundreds of years. A mask containing the desired
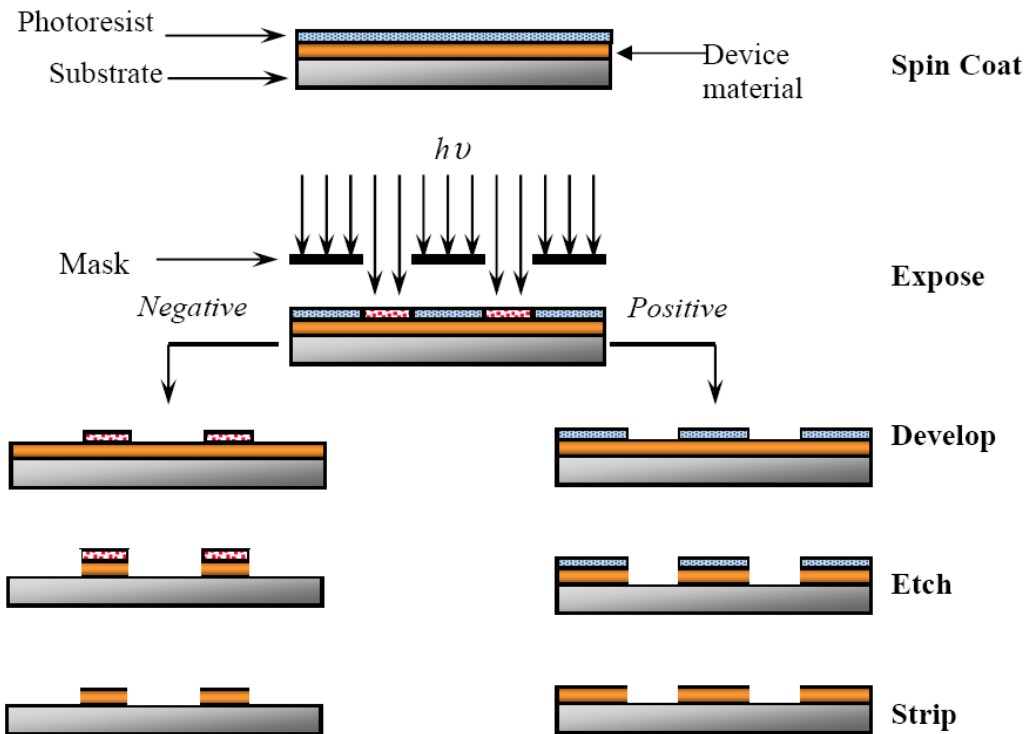
Figure 1.5: The projection lithography process entails a spin coat of photoresist material onto a bilayer substrate. The mask is held above this substrate and illuminated from the other side, so that it selectively illuminates the photoresist through the unmasked regions. A positive resist becomes soluble in the illuminated areas whereas the negative resist becomes insoluble in the illuminated areas. After the developer washes away soluble resist, an etch step transfers the pattern into the device material, and the photoresist can be stripped off to leave the patterned circuitry on the wafer.

8

pattern is held above a substrate and the mask is illuminated, selectively illuminating the substrate and creating a chemical change in those regions.

The photomask is made using a transparent glass or quartz plate that is covered with a thin metal layer. The metal is etched using laser patterning techniques. The metal is chosen based on the wavelength of the exposure light, so that the metal absorbs the light used for exposure of the photoresist beneath, with the photoresist layered atop the silicon wafer as shown in Figure 1.5. Thus, the photresist chemically changes only in the areas where the light has transferred through the mask. A negative resist becomes insoluble where light has exposed it, whereas a positive resist becomes more soluble in the illuminated areas. After exposure, the photoresist is immersed in a developer solution that dissolves the soluble areas, thus leaving photoresist in either the negative or positive pattern that was on the photomask. This pattern is used as an etch barrier or a doping barrier to keep the region of silicon (or other layer) beneath from being etched or doped. Once these steps are finished, the silicon can be removed to reveal the patterned semiconductor.

These basic lithographic steps have changed very little since the beginning of the electronics industry. As more circuits and ever more complex patterns have been loaded onto these wafers, the industry has had to be creative with modifying this basic method to make these advances in size and resolution possible.

1.4a. Photolithography: Contact, Proximity and Projection Lithography

The photolithography process is so called because of its use of illumination to create the pattern transfer between mask and substrate. There are several ways to implement this pattern transfer. The initial implementation was known as contact lithography, where the photomask was literally put on top of a silicon wafer with the layer of photoresist ready for patterning. The light was then projected through the mask and into the photoresist. The shortfalls of this method soon became apparent; the contact was causing the photomask to buildup dust and residue that was compromising the quality of images after many cycles of contact with wafers.

The clear solution to this issue in contact lithography was to separate the mask and wafer by a short distance while projecting the light through the mask, known as proximity lithography. This method suffered from resolution problems due to the close range of projection, which caused significant Fresnel diffraction, a type of diffraction that
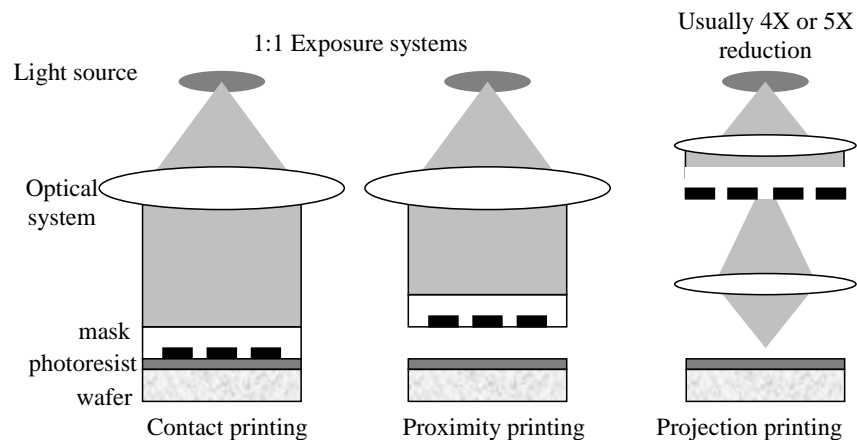
Figure 1.6: Conceptual schematics of contact, proximity and projection printing. Projection printing uses a lens between the mask and substrate for pattern reduction of up to 10X.

dominates at short distances between the mask and image planes. With a theoretical resolution limit of 1 micron, this method was eventually scrapped in favor of projection lithography, where lenses could be used on both sides of the mask to focus the light onto the image plane. The schematic comparisons are shown in Figure 1.6. This distancing of the mask from the image plane allows the process to move away from the Fresnel diffraction limit and into the Fraunhoffer diffraction regime, where theoretical resolution could be much smaller, depending on the Numerical Aperture of the lens, *NA*, the exposure wavelength λ, and a constant for the system k, which can vary from 0.6 to 0.8 depending on the shape of the opening in the mask and the resist properties [2]: $R_{min}=k\lambda/NA$.

The first implementation of projection lithography was a scanning process in which the illumination source produced a slit of light that scans the mask and reproduces the pattern in the wafer at a 1:1 ratio. As chips became more complex and wafers became larger, it made more sense to come up with a method for local alignment on particular areas of the wafer, called die, with a large mask that could be reduced in the image pattern. This system used reduction lenses between the mask and wafer to allow reduction in pattern size by as much as 10X. These systems exposed just a die at a time, stepping from one die to the next in a step-and-repeat fashion. This method was clearly advantageous for the low cost and high accuracy involved in mask making, since the masks could be kept large, thus easier to make and fix, and smaller lenses could be used that had inherently higher numerical apertures, yielding better resolution and fewer defects. This projection method is essentially the method in place today for

11
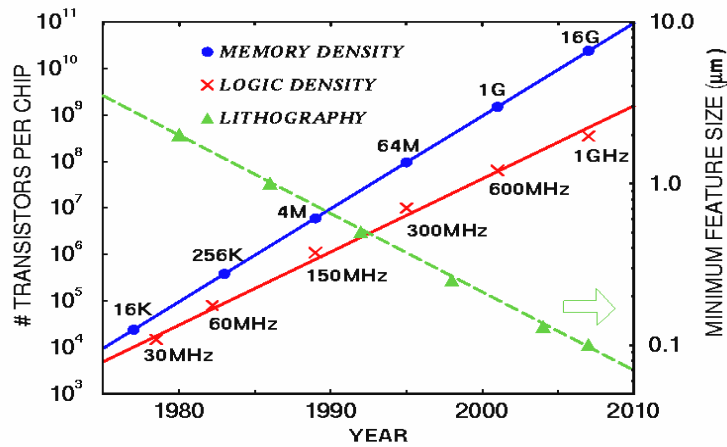
Figure 1.7: Exponential growth of memory density and microprocessing
power per die (area on chip) from microelectronic industry processors.

photolithography circuit fabrication. Improvements to this process have been necessary

for this ever advancing industry. In 1965, only a few years after the commercialization of

the integrated circuit for the electronic industry, Gordon Moore, the founder of Intel,

predicted that the density of components on a chip would double every year [3]. Though

his prediction was based on only 3 data points, it essentially held true for the first ten

years of the industry. In 1975 he gave an updated prediction in a speech to the IEEE

(Institute of Electrical and Electronics Engineers) that the trend would slow to a density

doubling occurring every 3 years [4]. In order to keep on track with this trend, the

International Technology Roadmap for Semiconductors (ITRS) was created by the

electronics industry. Figure 1.7 depicts the advances in lithography, depicting the

exponential increase in memory density on a die area as well as exponential decrease in

feature size, which is predicted to break through to the nanometer scale in the coming

years.

12
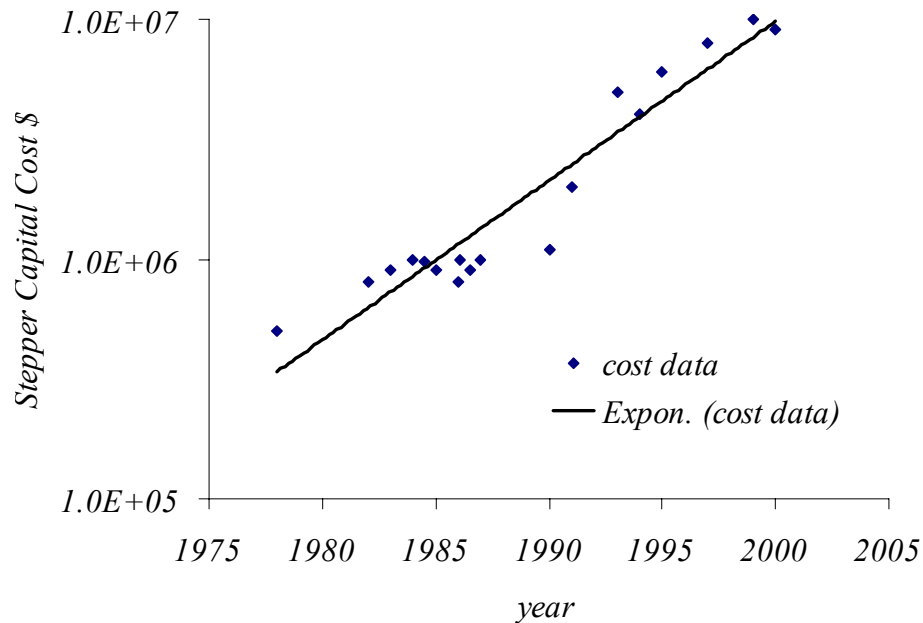
Figure 1.8: As the density of components on a chip has increased exponentially so has tool cost, with modern lithography tools costing close to ten million dollars. If the trend continues, possible costs for next generation tools such as EUV or SCALPEL tools could cost over ten million dollars; SFIL tool cost is well below the ten million dollar mark, making it an excellent alternative to the current trend.

Though physical limitations have continually seemed insurmountable, the industry has kept up with the trend; even now, where systems have been pushed to an optical limit (feature size resolution is fundamentally limited by the wavelength of light used for exposure), few people doubt that the technology will move forward. The more worrisome aspect is whether the technology will be affordable for manufacturing and commercial use. The industry is now at the point where the enhancement of already high cost projection systems are making future advances seem economically unfeasible. In fact, the cost of lithographic tools has been increasing exponentially along with the increase in component density [5] as shown in Figure 1.8 [6], with tools reaching the ten million dollar mark.

Techniques currently being investigated, including immersion lithography, deep UV and x-ray illumination, and SCALPEL (Scattering with Angular Limitation in Projection Electron-beam Lithography), all continue to use the projection method of past systems with even more expensive requirements. This economic barrier to achieving the next generation in circuit fabrication has pushed the industry to look for alternatives to the projection process.

1.4b. Electron Beam and Focused Ion Beam Lithography

As a starting point, maskless technologies that circumvent the need for projection through a patterned mask have been considered. Electron beam lithography uses a high energy column of electrons to pattern a substrate; while resolution is limited due to the proximity effect, where dimensions of the image are larger than the diameter of the beam due to the scattering of the electrons, this method is still capable of producing nanometer scale features. This is due to the fact that the wavelength of electrons is many orders of magnitude shorter than visible light, so that electron beams are not limited by their wavelength as are current projection systems.

The focused ion beam technique uses a liquefied metal source to generate a beam of ions that, if focused by an electromagnetic field, can generate a high energy column of ions that can be focused into a beam with a diameter also on the nanometer scale. Since the ions have wavelengths more than a million times shorter than visible light, these systems are not wavelength limited. While the ion beam does not suffer the proximity effect that exists in electron beam imaging, it tends to have limited efficacy in non-metal materials due to the charge buildup it creates in those materials that eventually repel the

ions from the beam and defocus the beam.

These methods have proven to be useful in other stages of fabrication, such as patterning the photomask and doping the semiconductor. Their time consuming nature and limitations, however, prevent use for large scale patterning. Alternatives have been suggested that combine the two methods, thus mitigating their individual limitations, but so far no fabrication tool has successfully been adopted by industry for large scale manufacturing due to the time intensive nature of these methods.

1.4c. Nanoimprint Lithography

The potential use of the electron beam writing process for generating high resolution nanometer scale features cannot be discarded based on its time consuming and expensive nature. The use of electron beams to pattern a mask that can then be reproduced many times, exactly as the photomask is reused many times in the photolithography process, has been the key idea behind nanoimprint lithography, depicted in Figure 1.9. While photolithography reproduces the mask pattern by imaging a photoresist via illumination through the mask, nanoimprint lithography reproduces the mask pattern by mircomolding, *i.e.* imprinting, a photo-curable or thermally curable polymer to reproduce the pattern. Thus, the pattern must be etched into the mask (often called a template in imprint applications, since it is essentially a stamp with a relief pattern that acts as a template for creating the relief pattern in the substrate). This process does away with expensive optics systems in favor of a much more affordable stamping process that is still high throughput if implemented in the same step-and-repeat fashion as
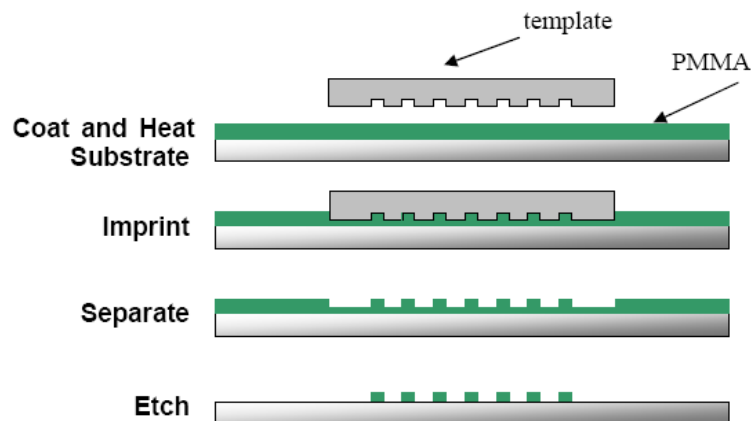
Figure 1.9: The nanoimprint lithography process.

traditional photolithography tools function.

The first molding process that succeeded in replicating a patterned template without destroying the template was called "micromolding in capillaries" (MIMIC) [7]. This method produced microscale features by using capillary filling for long channels. One of the first nanoimprint processes to replicate nanoscale features, developed by Chou et al.[8], was achieved using a thermally activated polymer layer as the transfer layer for patterning. The silicon substrate is spin coated with etch barrier material, typically PMMA (poly-methylmethacrylate) but possibly another thermally activated polymer, that is heated above its glass transition temperature and then imprinted with a template containing the desired relief pattern. After cooling, the template can be separated to reveal the patterned polymer layer. A breakthrough etch must be performed to remove the base layer of polymer, typically done by a reactive ion etch. This will reveal extremely small features, as small as 25 nm [9].

1.4d. Step and Flash Imprint Lithography

While these nanoimprint methods were successful in producing nanometer scale features, the high temperatures and pressures required for the thermal imprint process (as large as 140C and 1900 psi) were much too extreme for fabrication of multi-layer devices, with several levels of circuitry. The heating and cooling also took too much time to be viable as a high throughput manufacturing method. Thus, an alternative imprint process that would not require these extreme process conditions was sought by researchers at The University of Texas at Austin [10]. Here, inspiration came from a process at Phillips for making compact disks that used a photocurable monomer as an

17

imprint layer rather than the thermal polymer solution used in other imprint processes. The so called 2P process at Phillips [11] , which in fact was developed by Haisma *et al.* at the same time as Chou's thermoplastic imprint process, used a transparent template to imprint the monomer along with a flash of UV light to cure it so that it held the template shape. This monomer, being of lower viscosity than the polymer solution and liquid at room temperature, made the imprint step viable at mild processing conditions of room temperature and atmospheric pressure.

The SFIL process is outlined in Figure 1.10. It begins with a spin coat of transfer layer on the silicon wafer. This transfer layer is used for producing high aspect ratio features later in the process. Drops of silicon containing photopolymerizable imprint resist are dispensed onto the transfer layer. The template is then brought down toward the wafer and presses the drops so that the drops fill the gap between template and substrate, filling the relief pattern in the template. When the desired base layer is achieved, the pressing stops and the system is illuminated with UV light through the
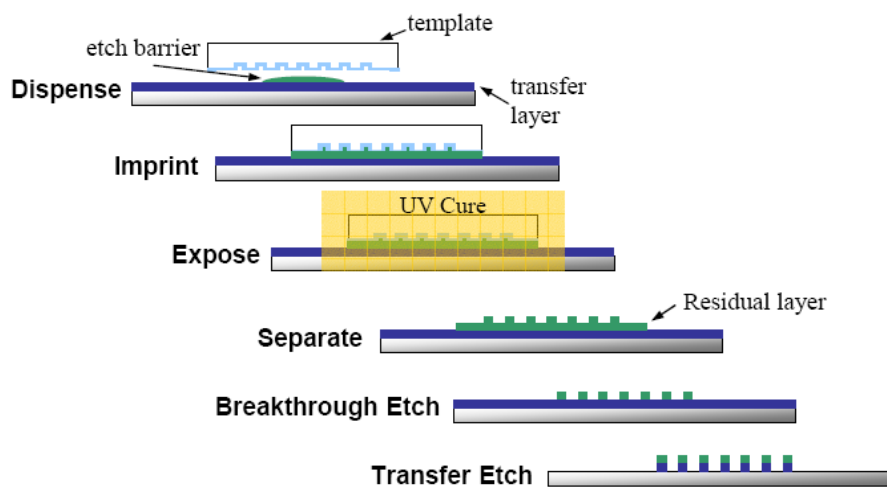
Figure 1.10: The step and flash imprint lithography (SFIL) process.
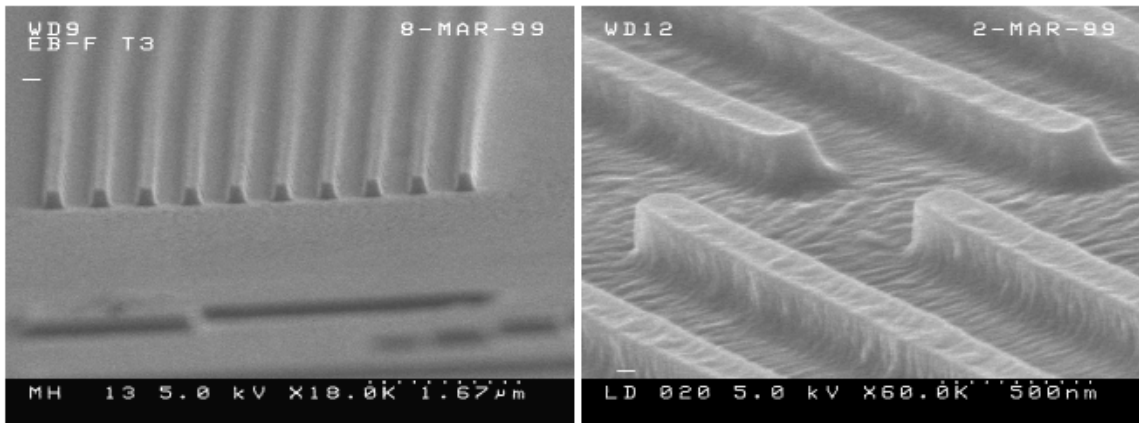
Figure 1.11: Line patterns produced by the early version of the SFIL process.

transparent (typically quartz) template. This cures the monomer into a crosslinked polymer form, and the template can be lifted off. Like the thermal imprint process, a residual layer of polymer is left behind, so a breakthrough etch must be done to reveal the underlying organic transfer layer. This transfer layer can then be selectively etched using oxygen (the silicon in the monomer keeps it resistant to the oxygen etch), thus breaking through to the substrate.

Figure1.11 shows images of line patterns formed from an early SFIL process. Still in its early stages, the SFIL process is developing with initial work on basic electronic circuits that will soon lead to attempts to fabricate complex CMOS circuits. There are several challenges that lie ahead on the road to commercialization of this process; because the template is a 1X replica of the imprint pattern, its features are much smaller than features on the 10X photomasks currently used in the industry, making mask repair a much more difficult task. The cost of the mask is also significantly more than a typical photomask, due to the expense and time intensive nature of e-beam writing

19

as well as the relatively large patterning area for the 1X template. Despite these issues, the technology is promising due to its ability to create nanoscale features at a fraction of the overall cost of other next generation lithography tools, with tool cost predicted to be well below the ten million dollars expected for competing processes. Research is rapidly moving forward both in industrial and academic research environments to bring this technology to the market.

This dissertation will focus on the imprint step in the SFIL process. Chapter 2 details the fluid dynamics involved in the monomer drop filling process, including the governing equations for the fluid flow and the implications of template control schemes such as constant velocity and controlled force imprinting. Chapter 3 explores the relationship between the solid mechanics of template deformation as caused by pressures exerted by the monomer layer. Chapter 4 gives a description of the complex interface motion that the monomer-air interface undergoes during the fill process, particularly the interface reconfiguration phenomenon that occurs as the interface moves through sharp features.

1.5. Conclusion

This century has seen astounding progress in electronic device fabrication and manufacturing since the first evidence of the existence of electrons was published. With discoveries including the transistor and the integrated circuit, scientists have found ways to harness the power of electron flow. Applications have ranged from radio and other long range communications and cookware such as toasters and microwaves to complex supercomputers with the capacity to do billions of mathematical operations in fractions of

a second. These commercial applications have been enabled largely by the process revolutions in manufacturing electronic circuits and the continually increasing number of components on a chip. The lithography process that has made this possible has undergone many improvements and adjustments since its inception, and there are more breakthroughs yet to come.

The barriers faced by the photolithography process in terms of physical limitations in optical methods as well as economic barriers in current technologies are leading the scientific community to invest in new technologies. The promise of nanoimprinting processes to overcome the physical and economic barriers facing the industry's ability to advance is worth the investment of time and effort of today's scientific research community. The SFIL process in particular shows significant potential due to its ability to produce sub-100 nm features under favorable processing conditions and affordable cost.

1.6 References

[1] J.J. Thompson, Naubel Laureate speech, nobelprize.org

[2] J.D. Plummer, M.D. Deal, P.B. Griffin, Silicon VLSI Technology: Fundamentals, Practice and Modeling, Prentice Hall, Inc. Upper Saddle River NJ, 2000.

[3] G.E. Moore, Electronics 38 (1965) 113-117.

[4] G.E. Moore, Proc. IEEE Digital Integrated Electronic Device Meeting (1975) 11-13.

[5] D.J. Resnick, W.J. Dauksher, D.P. Mancini, K.J. Nordquist, T.C. Bailey, S.C. Johnson, N.A. Stacey, J.G. Ekerdt, C.G. Willson, S.V. Sreenivasan, N. Schumaker, J. Vac. Sci. Technol. B 21 (6) (2003) 2624-2631.

[6] K.H. Brown, "Economic Challenges on the Path to 22nm", Future Fab International 17 (2004).

[7] E. Kim, Y.N. Xia, G.M. Whitesides, "Polymer microstructures formed by molding in capillaries", Nature 376 (1995) 581-584.

[8] S.Y. Chou, P.R. Krauss, P.J. Renstrom, "Imprint lithography with 25-nanometer resolution", Science 272 (1996) 85-87.

[9] Chou, S.Y.; Krauss, P.R.; Renstrom, P.J. "Nanoimprint lithography," J. Vac. Sci. Technol. B 14 (6) (1996) 4129-33.

[10] M. Colburn, T. Bailey, B.J. Choi, J.G. Ekerdt, S.V. Sreenivasan, C.G. Willson Solid State Tech. 44 (7) (2001) 67-75.

[11] J. Haisma; M. Verheijen; K. Van der Huevel; J. Van den Berg.; J. Vac. Sci. Technol. B. 14 (6) (1996) 4124-29.

Chapter 2: Simulation of Fluid Flow in the
Step and Flash Imprint Lithography Process

2.1. Introduction

The Step and Flash Imprint Lithography (SFIL) process offers a high-throughput, low-cost alternative to modern methods of lithography [1,2]. It avoids the use of costly optical systems for traditional projection printing and photolithography methods; instead, by using pattern transfer from masks made by electron beam writing, an image can be directly transferred to a substrate quickly and with much less expense than the electron beam writing of the mask itself. Electron beam lithography produces a high quality image with nanometer scale features, but it is much too slow and expensive to be a viable method for chip manufacturing. Reproduction of this mask image by imprint lithography is, however, a potentially fast method using low cost tools that makes possible the manufacturing of high quality chips with nanometer scale features [3].
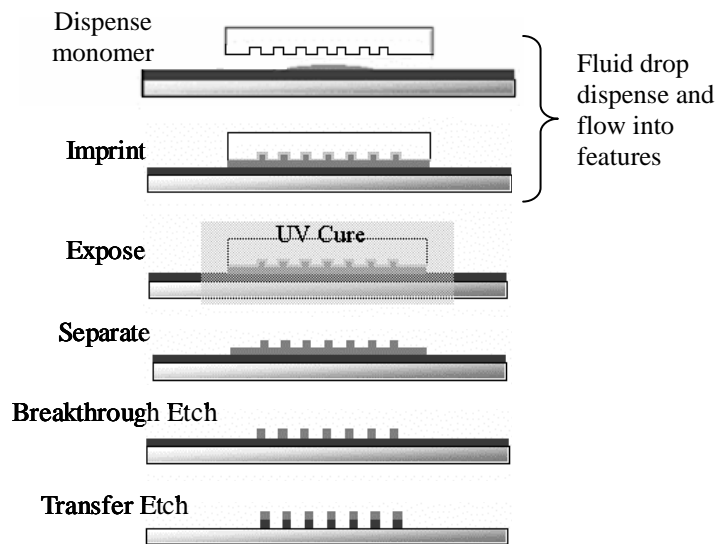
Figure 2.1: Steps involved in the SFIL process. The effects of drop dispense and fluid flow through template features are investigated in this Chapter.

The SFIL process is illustrated in Figure 2.1. Etch barrier in the form of a liquid monomer is dispensed onto a treated Silicon wafer. The monomer may be dispensed, for example, using a piezoelectric pump that delivers several fluid droplets in a chosen pattern onto the substrate. Typically, the final resist layer is approximately 50 nm thick over a one-inch square imprint area. For an initial dispense of five equal size drops, the initial drop radii would be about 450 μm with a height of 20 μm at the center, assuming the monomer wets the wafer surface with a five degree contact angle. The monomer drops are pressed into the shape of the quartz mask by bringing the template down with a given speed or applied force; the chosen velocity or force may determine how well the monomer fills features in the template. The amount of time allowed for the actual imprinting as well as the force applied to the template will determine the base layer thickness of monomer on the substrate. Ideally, the drops merge and fill the template perfectly. The resulting mold is then "flashed" with UV light through the quartz template to photopolymerize the monomer. After the removal of the mask, the resulting polymer is etched through the base layer to produce the high aspect ratio features that make up the desired structure on the wafer surface. Features as small as 10 nm with 1:1 aspect ratios (before the etch) have been produced using this imprinting process [4]. Figure 2.2 shows an example of such features.

While Thermal Imprint Lithography (TIL), has also been successful in producing nanometer scale features [5,6,7], the procedure is much more time consuming and not as well suited for high-throughput, large-scale production of patterned wafers. In the TIL process, the wafer is coated with the polymer form of photoresist and the imprinting is

24

performed above the polymer's glass-transition temperature. The pressures required for imprint are typically quite large in TIL, reportedly as high as 1900 psi, much higher than pressures used in SFIL; these high pressures can lead to significant template deformation[5]. The imprinting of a single layer of the highly viscous polymer form of the photoresist is not as effective as imprinting the liquid monomer, for which the lower viscosity fluid, use of multiple drops, and the advantage of capillary wetting allows for shorter imprint times [8].

Fluid dynamics is an important issue in the SFIL process. There is clearly a need for understanding the parameters that govern fluid flow of the liquid monomer between the substrate and the template. Issues that arise include the following: number of initial monomer drops and relative volume of drops dispensed, flow front arrest at edges of high aspect ratio features and template edges, air entrapment during feature filling, template velocity and force used for imprint, and imprint time.

In particular, this study explores the imprint time results for increasing numbers
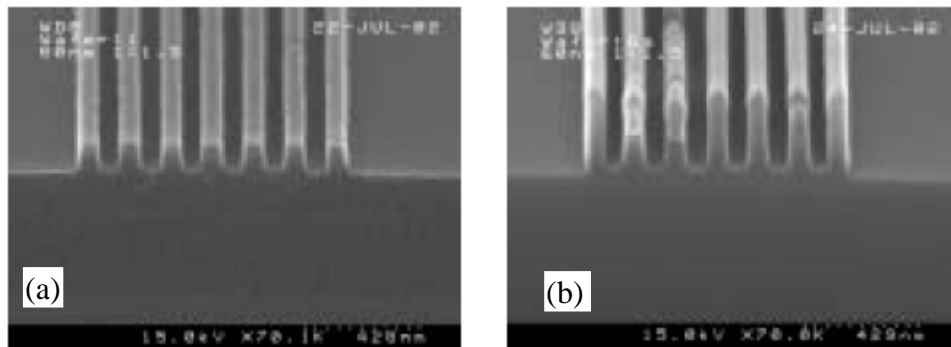
Figure 2.2: SEM images of line patterns printed by a current version of the SFIL process from Bailey *et al.* [3]; (a) 60 nm lines after imprinting, (b) 60 nm lines after etch processes.

of monomer drops and for various patterns of drop dispense for a perfectly rigid template. A comparison is also made of the use of an applied force on the template to the case where there is a net zero force on the template. For the latter instance, the attractive capillary forces between the template and wafer are allowed to exactly balance the repellant viscous forces generated during the imprint process. As will be seen, the use of a net zero force on the template is advantageous if template distortion is a concern since it leads to a lower pressure variation across the template. The filling of features on the scale of the drops, such as large contact hole features, is also presented in this study. Fluid leakage out of the imprint area is another issue of concern that is discussed.

2.2. Simulation

As the plates approach each other, the curvature of the fluid-air interface exerts a capillary force that pulls the template to the wafer due to the surface tension of the monomer and its wetting nature on both surfaces, as shown in Figure 2.3, where V represents the template velocity, R_0 is the initial drop radius, and h_0 is the initial gap height between the template and the wafer. Viscous forces exerted by the fluid balance this capillary force along with any applied force, F. The viscous forces arise from the fluid flow through the gap and the capillary forces arise due to the curved monomer-air

Curved fluid-air interface due
to wetting nature of fluid $\downarrow V, F$

h_0

R_0
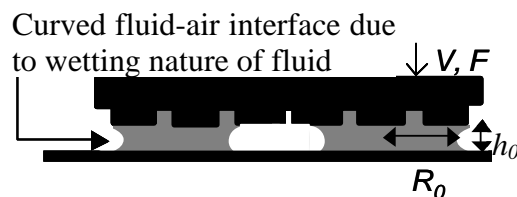
Figure 2.3: Cross section of template moving towards the substrate at velocity V or force F, pressing the monomer drops and causing them to spread through the channel.

interface that forms due to the wetting contact angles between the monomer and the plates.

Lubrication theory [9] allows simplification of the Navier-Stokes equations of motion for the case in which the gap height between the substrate and template is much smaller than the length scale of the drop. During the imprinting process, this is true due the relatively large size of the imprint area compared to the drop radii. Only at the end of the imprint process are the features significantly different in height compared to the base layer thickness; however, this irregularity is amended using a modified boundary condition, discussed shortly, and by the fact that volume conservation is rigorously ensured throughout the simulation. Thus, the following governing equations can be used to calculate the fluid's pressure and velocity field:

$$\nabla \cdot (H^3 \nabla P) = -12\mu V ,\qquad\qquad(2.1)$$

$$\mathbf{U} = \frac{-H^2}{12\mu} \nabla P ,\qquad\qquad(2.2)$$

where μ is the viscosity of the monomer, V is the downward velocity of the template, H is the gap height between the template and substrate at a given time in the process, P is the pressure in the fluid, and $\mathbf{U}$ is the vertically averaged, lateral velocity field. The boundary condition for solution of the lubrication equations accounts for the capillary force described. The pressure at the fluid air interface, $P|_{boundary}$, depends upon the dominant radius of curvature of the interface, which can be written in terms of contact angles and the gap height:

$$P\big|_{boundary} = P_{atm} - \gamma\left(\frac{\cos\theta_1 + \cos\theta_2}{H}\right), \tag{2.3}$$

where P_{atm} is the atmospheric pressure, γ is the surface tension, and θ_1 and θ_2 are the contact angles of the fluid with the template and the substrate, respectively. The contribution to the capillary pressure due to the other radius or curvature in the lateral direction or plan view of the template can be safely neglected since that pressure is $O(h_0/L)$, much smaller than that in Equation (2.3).

It is useful to non-dimensionalize the governing equations using characteristic values of the variables, namely $h_c = h_0$, $p_c = 12\mu VL^2/h_0^3$, and $u_c = VL/h_0$, so that $h = H/h_c$, $p = P/p_c$, and $u = U/u_c$. The lateral coordinates and ∇ operator are non-dimensionalized by L, the length of a side of the imprint area; h_0 is the initial gap height between the template and substrate. The resulting dimensionless equations and boundary conditions are given by

$$\nabla \cdot (h^3 \nabla p) = -1, \tag{2.4}$$

$$\mathbf{u} = -h^2 \nabla p, \tag{2.5}$$

$$p\big|_{boundary} = -\frac{1}{Ca}\frac{1}{h}, \tag{2.6}$$

where Ca is the dimensionless capillary number, which is given by

$$Ca = \frac{12\mu V}{\gamma(\cos\theta_1 + \cos\theta_2)}\left(\frac{L}{h_0}\right)^2. \tag{2.7}$$

The capillary number is the well-known ratio of the viscous force in the fluid to the capillary force caused by the surface tension of the fluid-air interface. A quantitative

understanding of the interaction of these forces is important for controlling the movement of the template. For typical values of the parameters, such as $\mu = 1$ cP, $V = 1$ μm/sec to 10 nm/sec, $L = 2.54$ cm, $\gamma = 30$ dyne/cm, and $h_0 = 1$ μm, the capillary number can range from 10^{-2} to 1.

The primary weakness of lubrication theory is that it presents the governing equations for fluid flow in only two dimensions and is strictly only valid for slow variations of the height of the gap in the z-direction. Thus, rapid fluid movement in the vertical direction, *i.e.*, into features on the template, cannot be explicitly tracked. In these cases the only way to predict fluid movement into a feature is to propose a mechanism for interface adjustment to fit into the feature. The discontinuous nature of such motion due to the sharp edges of the mask features, as shown in Figure 2.4, must be accounted for using adjustments in the boundary condition. A detailed analysis of this interface

A = $p_{initial}$

B, C = $p_{intermediate}$

D = p_{final}
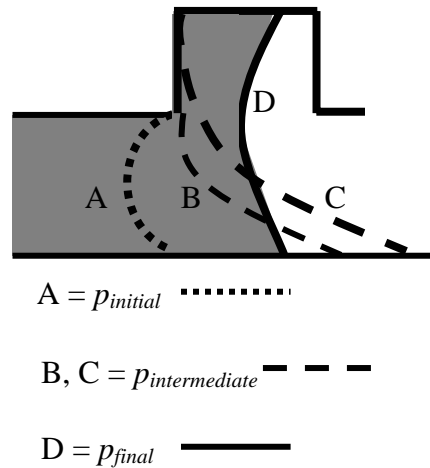
Figure 2.4: Fluid-air interface goes through unstable, stretched conformations as it rounds the feature corner, until there is enough fluid for the interface to move into a stable conformation inside the feature [10].

29

adjustment is presented in Chapter 4, but a brief description is useful here.

Interface conformation "A" in Figure 2.4 represents the interface just as it reaches the lower corner of a feature, where the boundary condition is a function of the gap height, h_{small}:

$$p\big|_{boundary} = p_{initial} = -\frac{1}{Ca}\frac{1}{h_{small}} \ .$$ (2.8)

For example, if the capillary number is equal to one and the gap height has closed to 5% of the initial gap height ($h_{small} = 0.05$), this initial interfacial pressure, $p_{initial}$, is –20. The interface then effectively pins to the first corner of the feature (B), as the upper contact line negotiates around the feature corner while the bottom contact line moves along the wafer surface. The upper contact line then moves vertically to the top corner of the feature, at which point the stretched interface (C) is able to reconfigure into a stable low surface energy conformation (D) [10]. This interface advancement cannot be explicitly modeled by 2D lubrication equations alone, but it may be represented computationally at first as a pressure buildup at the interface, with a no flow restriction imposed at the boundary as follows:

$$\mathbf{n} \cdot \nabla p_{intermediate} = 0 ,$$ (2.9)

where $\mathbf{n}$ is the normal vector of the interface; solving this equation for $p_{intermediate}$ creates a pressure buildup for the boundary pressure at the interface. The interface finally moves into the feature and resumes a stable conformation of lower surface energy when this intermediate pressure exceeds the final pressure inside the feature:

$$p_{final} = -\frac{1}{Ca}\frac{1}{h_{large}} ,$$ (2.10)

where h_{large} is the height inside the feature. For a feature of aspect ratio 2 at the final gap

height with h_{small} equal to 0.05, then h_{large} would be 0.1. Thus p_{final} is –10, a value greater

than the interfacial pressure $p_{initial}$. Once the pressure buildup is achieved, the interface

moves into the feature and fills the feature, and may be treated using the standard

capillary boundary condition once again. There is no similar retardation of the interface

for the case of flow from a large to small gap height, and so the standard pressure

boundary condition is applied.

Using finite differencing methods to solve these equations numerically allows the

calculation of the pressure and velocity fields in the fluid at a given time. The finite

difference scheme is of second order accuracy; the typical grid size is 200 by 200 cells,

for Δx=0.005, to ensure less than 1% mass loss. Simulations with up to 400 by 400 cells

were performed in order to verify numerical convergence for the smaller computational

grids. The Volume of Fluid (VOF) method [11] is used to move the fluid interface and

thus track the fluid movement accurately. The method requires tracking the volumes of

fluid in each cell in the numerical grid. Using velocity vectors on the faces of each cell,

fluid volumes can be updated by summing the fluid entering the cell and subtracting the

fluid leaving the cell at each time step. The time step size is determined by the maximum

velocity vector in the domain to avoid fluxing an amount of fluid greater than the size of

the cell:

$$\Delta t = \alpha \frac{\Delta x}{V \mid_{max}}, \tag{2.11}$$

where $V/_{max}$ is the maximum velocity vector in the grid and α is a fraction (usually about 0.2) chosen to ensure conservation of total volume. By defining the fluid-air interface at a given volume fraction, *e.g.,* cells that are half full, the fluid front can be tracked. Analytic expressions for the rate of a single drop spreading under a flat plate were used to check results from the simulation; strict volume conservation to within 1% is used to ensure valid results for all simulations. The process is assumed to occur in a vacuum or in a gas that is highly soluble in the monomer and so in the work discussed here, gas-trapping is neglected. The simulation is assumed to begin with fluid contacting both the substrate and template and immediate closure of the gap, so that evaporation of the monomer is neglected in the simulation. The computational time varied from three hours (for 1 drop) to a day (for 49 drops) on an Intel Xeon processor with 2.66 GHz clock speed and 2.07 Gb RAM.

2.3. Results and Discussion

Many of the following studies are presented for a zero net force on the template, in the case where viscous forces and surface tension forces balance exactly. In this case the characteristic velocity V must be determined by balancing these two forces. The characteristic viscous force is related to the viscous pressure,

$$F_V = p_c L^2 = \frac{12 \mu V L^4}{h_0^3},$$ (2.12)

and the characteristic capillary force is related to the capillary pressure,

$$F_C = \frac{\gamma(\cos \theta_1 + \cos \theta_2)}{h_0} L^2.$$ (2.13)

32

For these forces to balance, they must be equal, so that the velocity of the template has a characteristic value:

$$V = \frac{\gamma(\cos\theta_1 + \cos\theta_2)h_0^2}{12\mu L^2}, \tag{2.14}$$

Upon inserting this characteristic template velocity into the expression for the capillary number, the value *Ca=1* is obtained as our intuition might suggest, so that the following results are for simulations in which the template velocity is computed according to this force balance at a capillary number of one.

2.3a. Multiple Drop Simulation

Figure 2.5 illustrates the use of the VOF method for merging multiple drops under
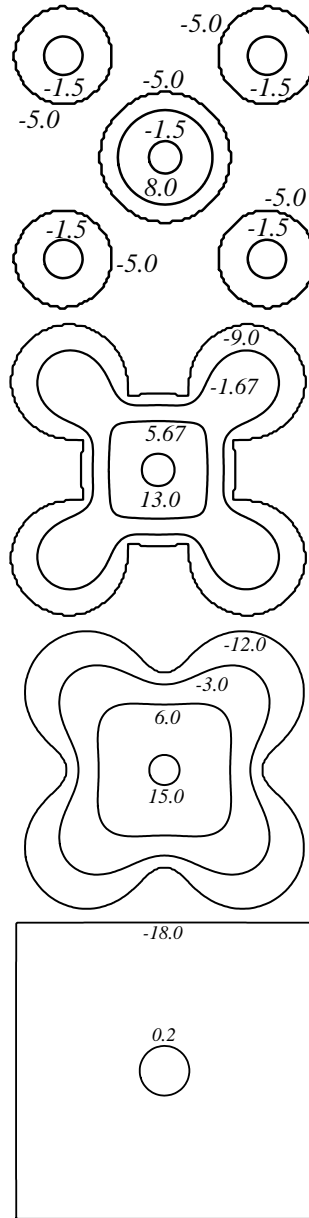
Figure 2.5: Pressure contours for merging of 5 drops at $t=0$, $t=0.02$, $t=0.06$, $t=1.05$ and $Ca=1$. The coalesced drops behave as a single drop with high interior pressure immediately after the drops merge. Lowest contour corresponds to fluid-air interface.

a flat plate at zero net force and a capillary number equal to one. The pressure contours show that the drops behave much as one large drop immediately upon the merging of the interfaces, with the pressure field exhibiting a maximum in the center of the imprint area. It is also clear that pressure contours near the center have a circular shape as they would for a perfectly round drop, no matter what the shape of the coalesced drops. This is shown, for example, in the case of the final pressure field where the drops have taken the square shape of the imprint area but the interior pressure contour looks similar to the initial case for circular drops. It should also be noted that the pressures are smaller toward the end of the imprint process due to the very negative capillary pressures at the fluid-air interface.

The interface curvature in this plan view is negligible compared to the interface curvature in the profile view, due to the disparate length scales over which these planes exist. The length scale of the plan view is from $L/h_0 = 10^3$ to 10^6 times as large as the height of the gap in the profile view over the duration of the imprinting process. Thus, though there may be moments when the interface curvature is significant in the plan view, such as the initial moment two drops merge, these instances are extremely brief, so that the curvature in the plan view may safely be neglected.

This multiple drop simulation was used to study multi-drop spreading and merging under a flat plate to obtain the subsequent results in this section. The simulations were performed for a net zero applied force, so that the capillary forces exactly balance the viscous forces. The initial sizes of the drops were chosen so that their

35

total volume would be equivalent to the final volume needed to fill a 50 nm gap between a flat template and wafer.

2.3b. Imprint Time

Simulations for increasing numbers of drops were performed for a template moving toward the wafer with zero applied force, the template velocity thus determined by balancing the capillary forces with the viscous forces. The results shown in Figure 2.6 illustrate clear decrease of imprint time for increasing numbers of drops.

The curves move toward the single drop case when the drops merge and behave as a single drop; this merge occurs at the same gap height, $h_{contact}=4h_f/\pi$, for any given number of drops with a total fixed volume, but the improvement in imprint time is still
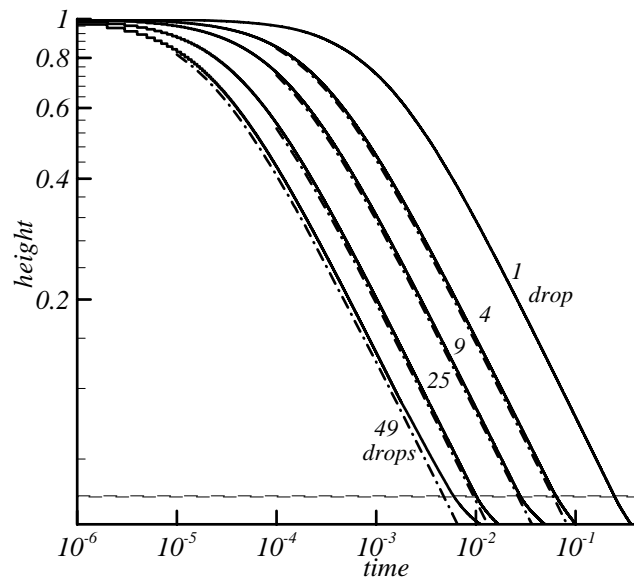
Figure 2.6: Imprint time for increasing numbers of drops, with mask velocity determined by balance of capillary and viscous forces. Dotted curves represent approximate analytic solutions from scaling analysis. Horizontal dotted line represents the height at which the drops merge.

36

apparent. For a characteristic time of $t_c=12\mu L^2/[h_0\gamma(cos\theta_1+cos\theta_2)] =129$ s, assuming θ_1 $=\theta_2=0$, the imprint time for one drop is 65 s compared to an imprint time of 1.5 s for 49 drops. Figure 2.7 illustrates the possibility of decreasing the imprint time by yet another order of magnitude by applying force to the template. The drawback in such a technique is that much higher pressures build in the fluid, on the order of 2.4 MPa as compared to only 450 kPa in the case of zero net force. This is an important consequence due to the issue of template deformation, which can occur if the pressures in the fluid are significant. While use of a net zero force alleviates high absolute pressures, it should be noted that large gradients in pressure could still exist, which can also contribute to template deformation. Deformations on the order of 70 nm for a 10 N force have been reported [12].

An approximate analytic solution is shown for each of the multiple drop cases,
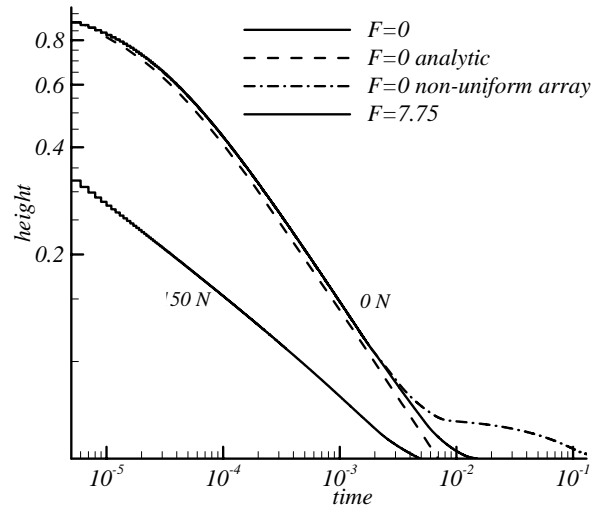
Figure 2.7: Imprint time for 49 drops in a square array. A non-uniform distribution of the drops leads to longer imprint time, while applying a force of 50 Newtons, corresponding to dimensionless value of 7.75, improves imprint time by a factor of 3.

where the capillary forces balance with the viscous forces. This analytic approximation can be derived along the lines discussed by Colburn *et al.* [9] by solving Equation (2.1) in its radial form for a single drop, namely

$$\frac{1}{r}\frac{\partial}{\partial r}\left(rH^3\frac{\partial P}{\partial r}\right) = -12\mu V .$$

(2.15)

With the boundary condition $P\big|_{r=R} = 0$, the pressure field is given by

$$P(r) = \frac{3\mu V}{H^3}(R^2 - r^2) .$$

(2.16)

Integrating the pressure field over the area of the drop yields the viscous force F_V,

$$F_V = \frac{3\pi\mu VR^4}{2H^3} .$$

(2.17)

The applied force on the template is the sum of viscous and capillary forces on all the drops; neglecting the force applied by the contact line itself, which is negligible compared to the area of the drops, the applied force is given by

$$F_{App} = \left[\frac{3\pi\mu VR^4}{2H^3} - \gamma\left(\frac{\cos\theta_1 + \cos\theta_2}{H}\right)\pi R^2\right]N ,$$

(2.18)

where N is the number of drops. Given the total volume of the N drops is $Q = \pi R^2 HN$, the velocity of the template is given by

$$V = -\frac{dH}{dt} = -\frac{2\pi}{3}\left[\frac{H^5 F_{App} N}{\mu Q^2} + \left(\frac{\hat{\gamma}}{\mu}\right)\frac{H^3 N}{Q}\right],$$

(2.19)

where $\hat{\gamma} = \gamma(\cos\theta_1 + \cos\theta_2)$.

Thus, there are two components that determine the template velocity; the first term on the right hand side of Equation (2.16) including F_{App} represents the applied force,

whereas the second term on the right hand side of Equation (2.16) represents the capillary forces.

The dominant case may be determined by comparing the forces. The applied force dominates if

$$\frac{H^5 F_{App} N}{\mu Q^2} >> \left(\frac{\hat{\gamma}}{\mu}\right) \frac{H^3 N}{Q},$$

(2.20)

or

$$\frac{H^2 F_{App}}{\hat{\gamma} Q} >> 1,$$

(2.21)

and the capillary force dominates if the contrary is true. Thus, there exist two asymptotic behaviors for the template velocity; each expression for the velocity may be integrated to obtain the relationship between the gap height and time. For the case in which applied forces dominate,

$$V = -\frac{dH}{dt} = -\frac{2\pi}{3}\left(\frac{H^5 F_{App} N}{\mu Q^2}\right),$$

(2.22)

or, nondimensionally,

$$V = -\frac{dh}{dt} = -8\pi f_{App} N \left(\frac{h_0}{h_f}\right)^2 h^5,$$

(2.23)

where $f_{App} = F_{App} \, h_0/[\gamma(cos\theta_1 + cos\theta_2)L^2]$. This expression may be integrated to obtain the height as a function of time to give,

$$h = \left[1 + 32\pi F_{App} N \left(\frac{h_0}{h_f}\right)^2 t\right]^{-\frac{1}{4}}.$$

(2.24)

39

This is the case in which a constant fixed force on the template causes the gap height versus time to decrease with a slope of -¼ on the log-log plot shown in Figure 2.7. Note that the analytic and numerical solutions for this case are indistinguishable.

For the case in which capillary forces balance the applied force, a similar integration of the velocity leads to:

$$V = -\frac{dH}{dt} = -\frac{2\pi}{3}\left[\left(\frac{\hat{\gamma}}{\mu}\right)\frac{H^3 N}{Q}\right],$$
(2.25)

or, nondimensionally:

$$V = -\frac{dh}{dt} = -8\pi N\left(\frac{h_0}{h_f}\right)h^3,$$
(2.26)

which may also be integrated to obtain an expression for the height as a function of time:

$$h = \left[1 + 16\pi N\left(\frac{h_0}{h_f}\right)t\right]^{-1/2},$$
(2.27)

where the gap height versus time decreases with a slope of -½ , as shown for the dotted line analytic approximations in Figure 2.6 and for the zero force cases in Figure 2.7. These analytic approximations correspond extremely well to the simulation results, until the point where the drops merge and behave as one single drop, therefore moving away from the analytic approximation. If the drops are not placed in a uniform array in the imprint area, the drops merge before the final imprint thickness has been achieved, causing an order of magnitude increase in the imprint time and potentially high pressures in the fluid.

2.3c. Feature Fill

Varying aspect ratios of features will exist; these features will fill based on the boundary condition presented in the simulation section. The pressure jump that the interface must undergo will vary based on the current base layer thickness as it compares to the height of the feature. For a feature of aspect ratio 2:1, where the feature height is twice that of the final base layer thickness, the feature fills with some lag time as compared to the area around it, as depicted in Figure 2.8(a). If the feature aspect ratio is
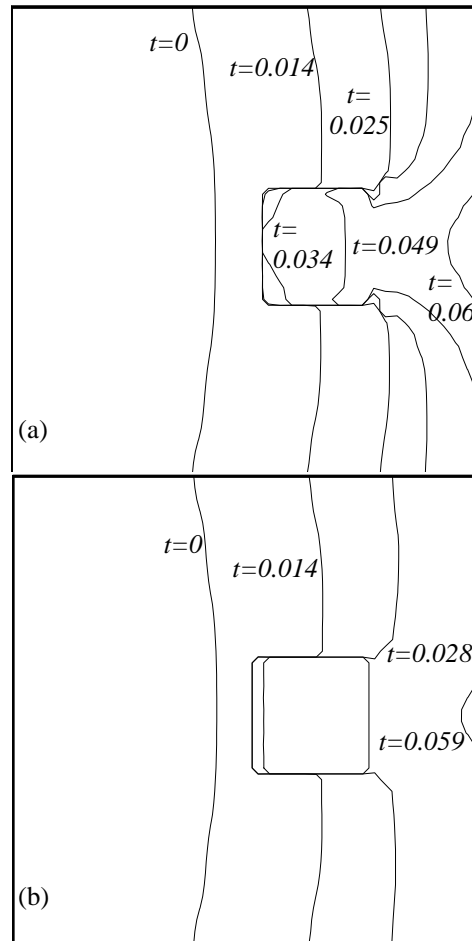
Figure 2.8: Fluid interface snapshots during the imprint. (a) Feature of aspect ratio 2:1 fills. (b) Feature of aspect ratio 2.5:1 does not fill.

increased slightly so that the feature is 2.5 times the thickness of the final base layer, i.e. 2.5:1 ratio, the feature does not fill, as shown in Figure 2.8(b). This is because the pressure buildup behind the front of the fluid is insufficient to break into the large aspect ratio feature for this particular simulation. These results are for a single drop spreading under an otherwise flat plate, with zero net force on the template and a capillary number equal to one. The feature length and width were 10% of the initial radius of the drop; results shown are for a very refined grid where $\Delta x=0.0025$, but the filling results for the features were the same for a less refined grid where $\Delta x=0.005$.

This technique can be used for any type of feature on the mask. Figure 2.9 illustrates a line pattern filled by 3 drops with a dimensionless applied force of 7.75; the lines, which have a width equal to 10% the initial diameter of the drops and an aspect ratio of 2:1, do not fill immediately if the fluid interface must move into the high pressure region; however, the portion of the lines where the fluid drops are placed fill easily due to the drop flow along the line.
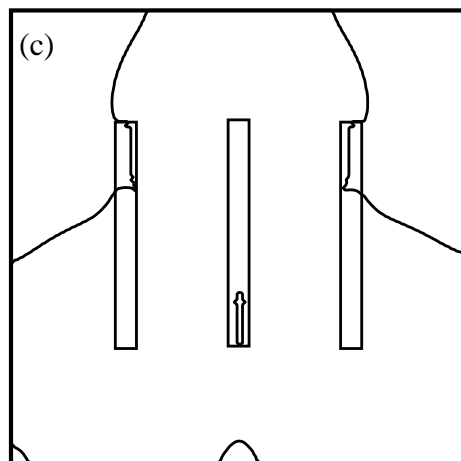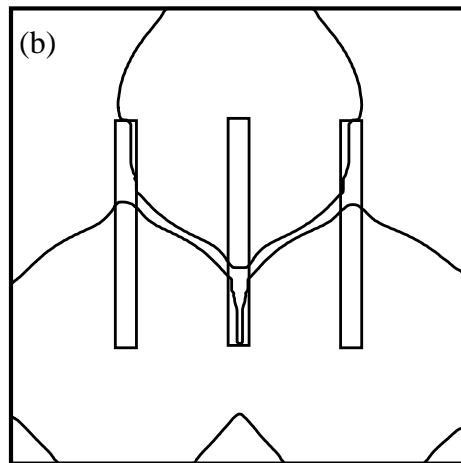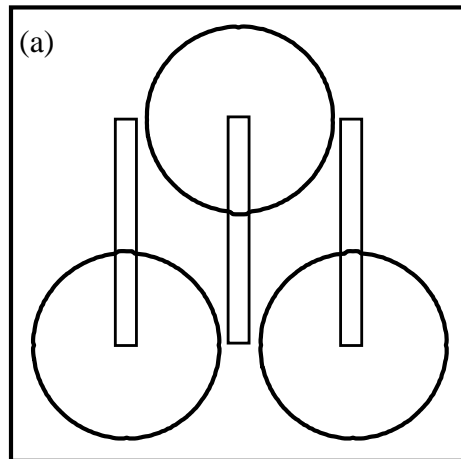
Figure 2.9: Fluid interface snapshots during the imprint. The hole formed at the bottom of the center line in (c) is eventually filled, assuming the surrounding medium is vacuum or highly soluble gas.

2.3d. Feature Density

In practice a template is composed of regions of high and low feature density, and the arrangement and size of droplets underneath can strongly affect the imprint time.
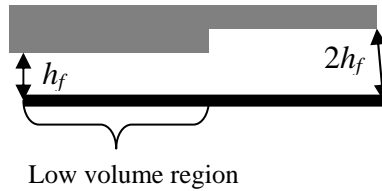
Figure 2.10: Final gap height, h_f, in low volume area is half that in the high volume area, as for an area of the mask where features are very dense.

In this case, areas on the mask with many features may be modeled as low volume areas, due to the presence of the features, as shown in Figure 2.10. Imprint time can be improved in such a situation by placing drops of lower volume in the feature dense area of the mask, such that the total volume of the drops in the low volume region is half the
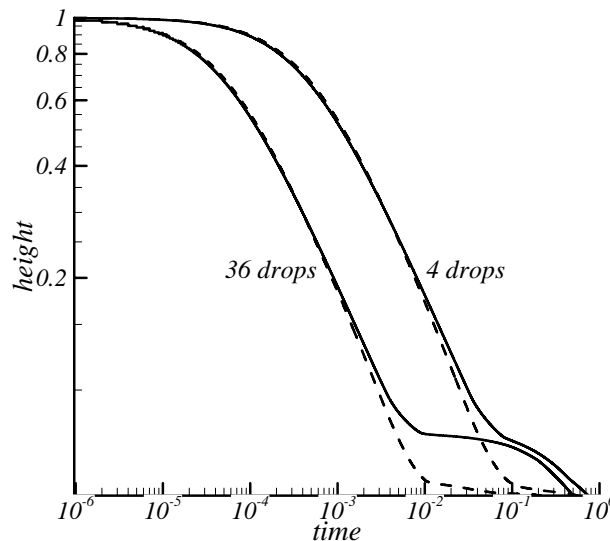
Figure 2.11: Dashed lines represent unequal volume drops, where smaller drops are used in the low volume region. This adjusting drop volume improves imprint time

volume of the drops in the high volume region. Imprint time results are shown in Figure 2.11. It is apparent that the drop merge occurs closer to the end of the process for unequal sized drops, resulting in shorter imprint times. Using the characteristic time t_c=129 s, the imprint time for 36 drops of unequal volume is an order of magnitude smaller, ~12 s, compared to the equal drop array or the 4 drop arrays, with imprint times of ~120 s.

2.3e. Mask Edge

For a single fluid drop spreading due to only the capillary action acting on a flat template (no applied force), the fluid does may or may not leak out of the mask edge. In general, the high aspect ratio of the mask edge confines fluid under the imprint area as seen in Figure 2.1. Fluid travels preferentially along the mask edge for these high aspect ratio edges; however, fluid loss at the mask edge occurs for a lower aspect ratio edge, if the aspect ratio is less than 2:1 as shown in Figure 2.12. The application of an applied
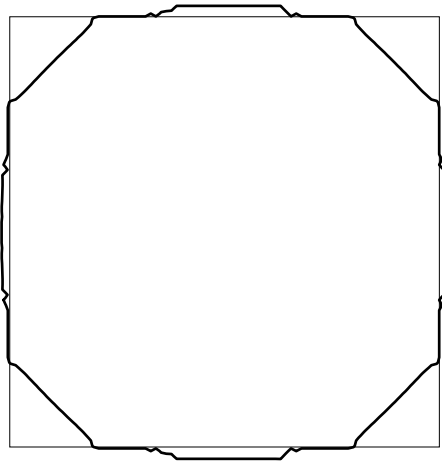
Figure 2.12: For edges of aspect ratio 2:1, fluid leaks outside the imprint area before the final base layer thickness is achieved.

45

force generally decreases the critical aspect ratio for fluid to leak out at the mask edge.

2.4. Conclusions

A dynamic, multi-drop simulation of fluid filling in Step-and-Flash imprint lithography has been presented. The foundation of the simulation is lubrication theory, which has been modified to handle flow into sharp features with a boundary condition that accounts for contact line dynamics at the corners of the features. The Volume of Fluid method is used to handle the merging of droplets and interfaces in the simulation.

Several fluid management issues critical to enhancing the speed and quality of the imprinting process were studied with the simulation. It has been shown that imprint time clearly decreases with the use of increasing number of droplets. An applied force on the template may significantly reduce the imprint time compared to capillary action alone, though the higher fluid pressures encountered could lead to template deformation. It has also been shown that the density of features and their position on the mask may affect the imprint time, highlighting the necessity for varying the volume of the drops based on their position over the imprint area. Modeling of individual features and the mask edge has been presented with the use of a modified boundary condition, and it is clear that high aspect ratio features impede filling. This simulation thus provides a valuable tool for the analysis and optimal design of the SFIL fluid filling process.

2.5. References

[1] T.C. Bailey, S. C. Johnson, S. V. Sreenivasan, J.G. Ekerdt, C.G. Willson, D.J. Resnick, J. Photopolymer Sci. Technol. 15 (3) (2002) 481-486.

[2] J. Haisma, M. Verheijen, K. Van den Heuvel, J. Van den Berg, J. Vac. Sci. Technol. B. 14 (1996) 4124-4129.

[3] T. C. Bailey, S.C. Johnson, M.D. Dickey, J.J. Smith, A.T. Jamieson, E.K. Kim, N.A. Stacey, D. Mancini, W.J. Dauksher, K. Nordquist, D.J. Resnick, S.V. Sreenivasan, J.G. Ekerdt, C.G. Willson, in: Proceedings of the 39th Interface Symposium, 2002.

[4] M. Colburn, A. Grot, M. Amistoso, B.J. Choi, T. Bailey, J. Ekerdt, S.V. Sreenivasan, J. Hollenhorst, C.G. Willson, Proc. SPIE 3997 (2000) 435.

[5] S.Y. Chou, P. R. Krauss, P.J. Renstrom, J. Vac. Sci. Technol. B. 14 (1996) 4129–4133.

[6] H.C. Scheer, H. Schulz, T. Hoffmann, S. Torres, J. Vac. Sci. Technol. B. 16 (1998) 3917-3921.

[7] B. Heidari, I. Maximov, E. Sarwe, L. Montelius, J. Vac. Sci. Technol. B. 17 (6) (1998) 2961-2964.

[8] M. Colburn, B. J. Choi, S. V. Sreenivasan, R. T. Bonnecaze, C.G. Willson, Microelectron. Eng. 75 (2004) 321-329.

[9] W.M. Deen, Analysis of Transport Phenomena, Oxford University Press, New York, 1998.

[10] S. Reddy and R.T. Bonnecaze, Phys. Fluids 17 (2005) 122104-1 – 122104-6.

[11] C. W. Hirt and B. D. Nichols, J. of Comp. Phys. 39 (1981) 201-225.

[12] S. D. Schuetter, G. A. Dicks, G. F. Nellis, R.L. Engelstad, E.G. Lovell, J. Vac. Sci. Technol. B. 22 (6) (2004) 3312-3317.

Chapter 3: Simulation of Template Deformation in the Step and Flash Imprint Lithography Process

3.1. Introduction

The Step and Flash Imprint Lithography (SFIL) process offers a high-throughput, low-cost alternative to modern methods of lithography [1,2]. Several next generation lithography technologies have been presented in both academic and industrial research, many of which avoid the use of costly optical systems, instead focusing on maskless methods such as electron beam and focused ion beam direct writing, or on printing methods known as imprint lithography. Imprint allows an image to be directly transferred to a substrate from a template that has been written (typically using electron beam writing for its nanoscale writing capability) with the pattern desired. Although this template is expensive to make due to the time consuming nature of the e-beam writing process, it can be used many times to reproduce the nanoscale pattern via imprinting, a
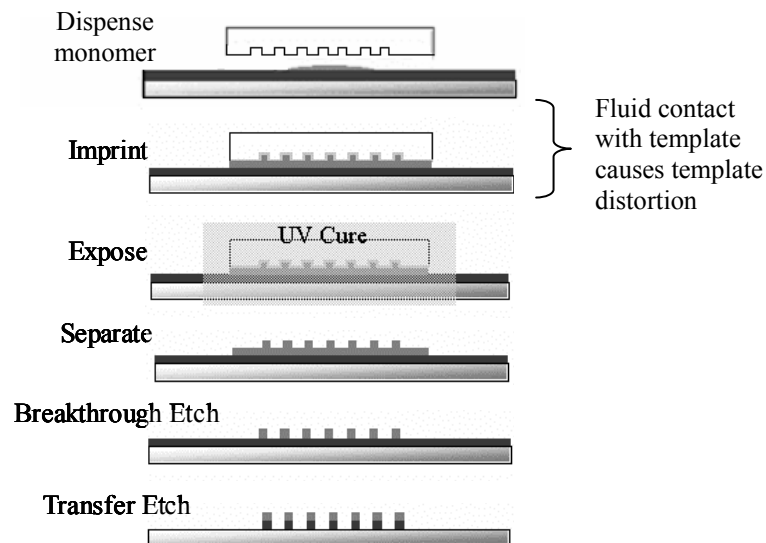
Fig. 3.1: Steps involved in the SFIL process. The circumstances under which fluid contact with the template lead to template distortion are investigated in this Chapter.

high throughput and low cost way to reproduce the template pattern [3]. The desire to reproduce nanoscale features requires an extremely thin base layer, typically 50-100 nm thick over a one inch square area, so that deformation in the template could be a significant problem in resolving these nanoscale features if the deformations are even just tens of nanometers in magnitude.

The SFIL process, illustrated in Fig. 3.1, involves pressing fluid in the template-substrate gap. As noted in our previous publication, fluid dynamics is an important issue in the SFIL process, having significant influence on imprint times and imprint pressures [4]. This study aims to gain insight into the effects of those imprint pressures on the template deformation encountered during the process. These deformations depend significantly on the imprint pressures encountered during the process, which can be both positive and negative due to the interplay of viscous and capillary forces.

Previous work by Scheutter et al. has shown that deformations can in fact be significant [5]. This previous study focused on the effect of one square drop spreading over an imprint area for given sets of process parameters, varying either fluid viscosity, template thickness, or template velocity. For these simulation parameters, positive distortions of 50-100 nm were shown to occur near the end of a constant velocity process.

A more advanced study of the imprint process is undertaken in this work, where we consider multiple circular drops spreading into a square imprint area and the effect on imprint time and imprint pressure. Instead of varying one or two individual process parameters, we capture the many process parameters in a nondimensional capillary number that provides deeper insight into the template deformation behavior under various

conditions. By varying the capillary number, this work will demonstrate that distortions depend significantly on any process parameter that is included in the capillary number.

3.2. Simulation

The simulation requires a coupled solution of the fluid and solid dynamics of the problem. The fluid dynamics are solved using the simplifying assumption of lubrication theory on the governing equations of motion, along with a boundary condition that includes the capillary pressure at the monomer-air interface, in the following non-dimensional forms [5],

$$\nabla \cdot (h^3 \nabla p) = -1 + \frac{\partial w}{\partial t}, \tag{3.1}$$

$$p\big|_{boundary} = -\frac{1}{Ca}\frac{1}{h}, \tag{3.2}$$

where Ca is the dimensionless capillary number, which is given by

$$Ca = \frac{12\mu V}{\gamma(\cos\theta_1 + \cos\theta_2)}\left(\frac{L}{h_0}\right)^2, \tag{3.3}$$

and where p is the pressure in the fluid, h is the gap height between the template and substrate at a given time in the process, w is the plate displacement as a function of lateral coordinates x and y, t is time, V is the downward velocity of the template, μ is the viscosity of the monomer, L is the length of the template, h_0 is the initial gap height between the template and substrate, γ is the surface tension, and θ_1 and θ_2 are the contact angles of the fluid with the template and the substrate, respectively. The contribution to the capillary pressure due to the other radius of curvature in the lateral direction or plan

50

view of the template can be safely neglected since that pressure is $O(h_0/L)$, much smaller than interface curvature in the profile dimension used in Equation(3.3).

The solid mechanics may be simulated using thin plate theory [6] for which the dimensional form of the equation is

$$DV^4W = P,$$
(3.4)

where capital letters denote dimensional forms of the variables. The criterion for using the thin plate equation is that the ratio of the plate length to its thickness is between eight and 80; if the ratio is greater than 80 the plate is considered a membrane and is devoid of flexural rigidity, and if the ratio is less than 8 the plate is considered a thick plate and must be modeled using general equations of three dimensional elasticity. In this study, the template length is assumed to be three times the length of the imprint area, which is typically one inch, and the template thickness is typically a quarter of an inch, so in this case the ratio of plate length to thickness is 12, which validates use of the thin plate equation. Equation (3.4) may be non-dimensionalized with the characteristic deformation, w_c, chosen to be the initial gap width, so that $w_c=h_0$. The characteristic pressure, p_c, is the same as for the lubrication equation, $p_c =12\mu VL^2/h_0{}^3$. Therefore $w=W/h_0$, where w is the nondimensional deformation, and $p=P/p_c$, where p is the nondimensional pressure. The ∇ operator is nondimensionalized by the template length L, giving :

$$\nabla^4 w = Ca\left(\frac{L^4\gamma(\cos\theta_1 + \cos\theta_2)}{Dh_0^2}\right)p,$$
(3.5)
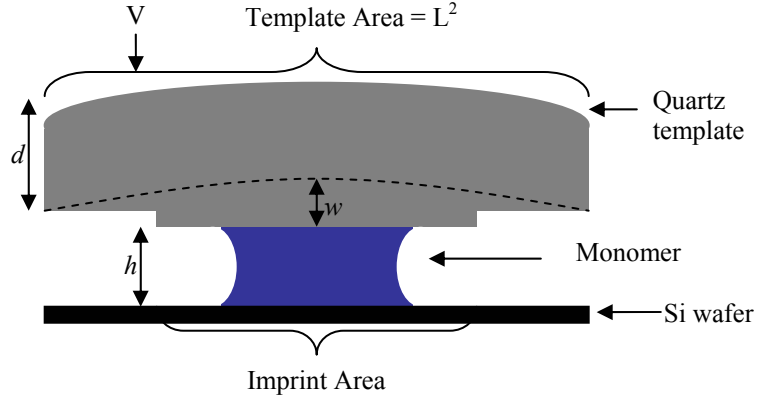
Figure 3.2: Schematic of the template-fluid-substrate profile. The template length is 3 times that of the imprint area, with the imprint area delineated by a step function in the gap height.

$$w\big|_{boundary} = 0, \tag{3.6}$$

$$\frac{\partial w}{\partial n}\bigg|_{boundary} = 0, \tag{3.7}$$

where n is the x or y direction and D is a constant involving material constants of the template,

$$D = \frac{Ed^3}{12(1-\upsilon^2)}, \tag{3.8}$$

Where E is the young's modulus, d is the plate thickness, υ is the Poisson ratio; using typical values for a quartz template, E=72.6 GPa, d=6.35 mm, and υ =0.16, D=1590 nm. A typical value for the nondimensional group in Equation (3.5) can be computed using γ =0.0225 N/m, L=2.54cm, h_0=1μm, θ_1 and θ_2=0, so that $\left(L^4\gamma(\cos\theta_1 + \cos\theta_2)\right)/\left(Dh_0^2\right)$=11.8. Figure 3.2 shows a schematic of the deformation, which occurs over the area of the template. The template's length is three times the length of the fluid imprint area.

Due to the coupled nature of this problem, in which the fluid pressure field determines the deformation field and likewise the deformation field affects the local height $h(x,y)$ that is needed to solve for the pressure field, an iterative solution scheme must be used to converge upon the correct solutions for pressure and deformation. The convergence criterion is that the solution for the deformation field is within 1% of the previous iteration. The computation progresses as follows: the pressure field is first computed using an initial $h(x,y)$ of one; this pressure field is used to compute a deformation field, which is used to adjust $h(x,y)$ and then the pressure field is recomputed using the new $h(x,y)$. This new pressure field results in a new deformation field, and if the new deformation solution is within 1% of the last iteration's solution, the time is advanced and the plate is moved by $V\Delta t$; if this convergence criterion is not met, the iteration is repeated until convergence is achieved. A relaxation parameter is used where the initial guess for the next iteration is a chosen percent of the current solution combined with part of the solution from the previous iteration in order to stabilize the computation. A computational grid with as many as 22,500 cells (150x150) is used, with mass conservation within 1%. Larger grids were used to compare results and ensure accuracy irrespective of the chosen grid size. Fluid-air interfaces are kept track of using the Volume of Fluid method [7], so that multiple drops can merge and form one outer interface. Computational time varied from 2 hours for simulation of 1 drop to 6 days for a 9 drop simulation; simulations were performed on an Intel Xeon processor with clock speed 2.66 GHz and 2.07 Gb RAM.

3.3. Scaling Analysis

It is useful to consider the relationship between the plate deformation and the constants involved in the imprint process, which can be derived from a scaling via order of magnitude analysis. The scaling of the deformation comes from the thin plate equation,

$$w \sim \frac{p_c L^4}{D},$$ (3.9)

where p_c is the characteristic pressure scale. This characteristic pressure could be the viscous pressure or the capillary pressure. The following analysis will give scaling predictions for both cases, under conditions where the template is moving either at constant velocity or via capillary suction. These predictions will be used to compare to and interpret numerical simulation results.

3.3a. Constant Velocity

For a constant velocity process, the characteristic pressure will scale as a capillary pressure at the beginning of the process, due to the suction of the wetting fluid that exerts a negative force on the template. This negative capillary pressure eventually gives way to the buildup of viscous pressure at the end of the process. Considering first the regime in which capillary forces dominate, the characteristic pressure scales with the capillary contribution from the pressure at the fluid-air interface,

$$p_c = p_{capillary} \sim \frac{\hat{\gamma}}{h};$$ (3.10)

This capillary pressure can be used in Equation (3.9) to obtain the minimum deformation

encountered by the template, i.e. the largest concave deformation due to the sucking force of the capillary pressure,

$$w_{min} \sim \left(\frac{L^4 \hat{\gamma}}{hD} \right). \tag{3.11}$$

Now considering the point at which the capillary pressure regime gives way to the viscous pressure regime by balancing the characteristic viscous and capillary pressures, so that $p_c \sim p_v$:

$$\frac{12 \mu V R^2}{h^3} \sim \frac{\hat{\gamma}}{h} \tag{3.12}$$

and writing in terms of the capillary number,

$$h \sim Ca^{1/2} h_0, \tag{3.13}$$

which can be used in Equation (3.13) to express w_{min} in terms of capillary number,

$$w_{min} \sim \left(\frac{L^4 \hat{\gamma}}{h_0 D} \right) \frac{1}{Ca^{1/2}}, \tag{3.14}$$

thus w_{min} scales as $Ca^{-1/2}$.

Considering instead a characteristic pressure that is based on the viscous contribution from the template's pushing force,

$$p_c = p_{viscous} \sim \frac{\mu V L^2}{h^3}; \tag{3.15}$$

this viscous pressure can be used as the characteristic pressure in Equation (3.9) to write an expression for the maximum positive deformation encountered by the template, written here in terms of the amount of fluid used Q, where $Q \sim hR^2$ and $R \sim L$ by the end of

55

the process, so that the positive maximum deformation by the end of the process is

$$w_{max} \sim \frac{\mu V Q^3}{h^6 D},$$ (3.16)

Or in terms of the capillary number,

$$w_{max} \sim Ca\left(\frac{L^4 \hat{\gamma}}{h_0 D}\right)\left(\frac{h_0}{h}\right)^3,$$ (3.17)

where $\hat{\gamma} = \gamma(\cos\theta_1 + \cos\theta_2)$. This scaling shows that w_{max} is linearly related with the capillary number and exponentially related to the gap height.

3.3b. Zero Force

For a zero force process, the plate is allowed to move only as fast as capillary pressure pulls it toward the plate, so that the capillary forces exactly balance with viscous forces, resulting in a net zero force. Using the lubrication equation, Equation (3.1), where p_c scales as a capillary pressure and assuming that $h >> w$, so that the $\partial w / \partial t$ term in the lubrication equation can be neglected,

$$\frac{h^3}{\mu R^2}\frac{\hat{\gamma}}{h} \sim V \sim \frac{h}{t},$$ (3.18)

Rearranging in terms of h,

$$h \sim \left(\frac{\mu Q}{\hat{\gamma} t}\right)^{1/2},$$ (3.19)

which is useful in scaling the deformation equation, Equation (3.9), using the capillary pressure as the characteristic pressure and substituting h with Equation (3.19):

56

$$w \sim \left(\frac{Q\hat{\gamma}^5}{D^2\mu^3} \right)^{1/2} t^{3/2} . \qquad (3.20)$$

These scalings prove to be useful in interpreting results from simulation, and these relationships will be verified and compared to numerical results in the following sections.

3.4. Simulation Results

3.4a. Constant Velocity – Single Drop

A constant velocity scheme for the moving template was simulated for imprinting conditions at varying capillary numbers, from Ca=0.1 to Ca=10. Plot of the deformation, w, in Figure 3.3(a) shows that for increasing capillary number, template deformation becomes more positive. This is due to the increasing viscous pressure encountered in the
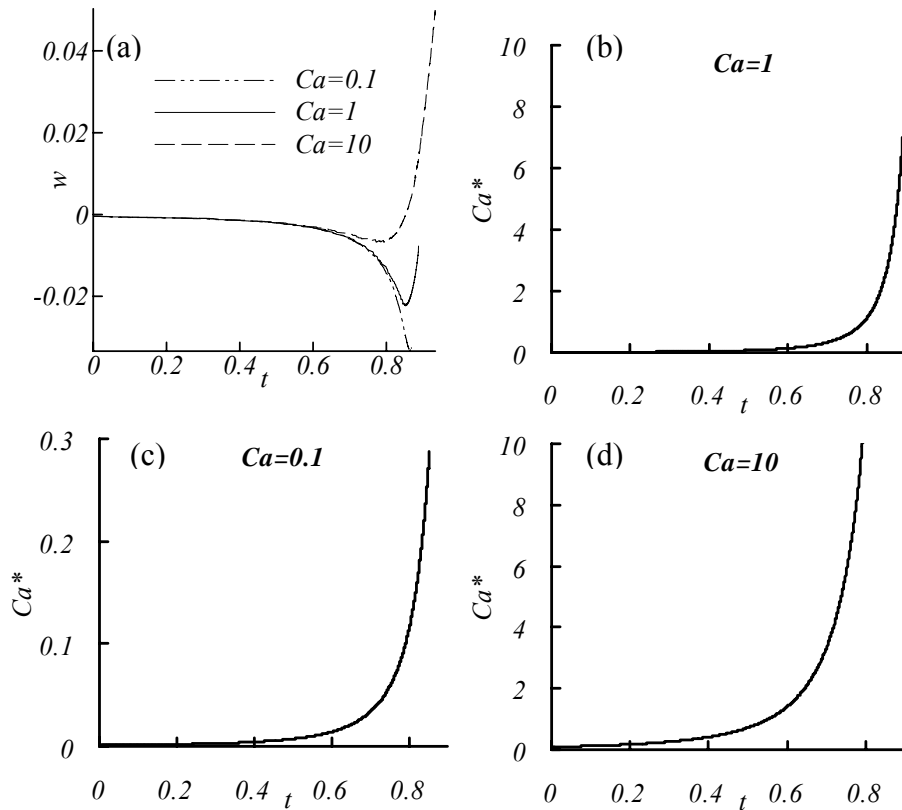
Figure 3.3: Simulations results for the deformation incurred by a template moving at constant velocity. (a) Results for varying capillary numbers; (b) For Ca=1, Ca^* transitions to greater than one at t~0.8, corresponding to the shift seen in plot (a) for this capillary number; (d) For Ca=0.1, Ca^* never transitions to greater than one, corresponding to plot (a) in which Ca=0.1 remains in the capillary dominated regime throughout the simulation; (d) For Ca=10, a transition to the viscous regime should occur for t>0.6, corresponding to the time when w departs from the other curves in plot (A) for Ca=10, transitioning to more positive deformations.

58

center of the drop for higher capillary number; while a process for Ca=0.1 operates in an entirely negative pressure regime, creating a sucking force that deforms the template in a concave manner measured by a negative value for w, a process for Ca=1 or greater operates between the negative and positive pressure regimes, so that an initial sucking force creating concave deformation is replaced by a repellant viscous force that creates a convex deformation measured by a positive w value. Values for the deformation can be multiplied by the characteristic w, h_0, to obtain dimensional values. Using h_0=1micron, the final deformation for Ca=10 is w_{final}= 50nm, for Ca=1 w_{final}= -5nm, and for Ca=0.1 w_{final} =-33nm.

A modified capillary number for the process can be defined by using the volume
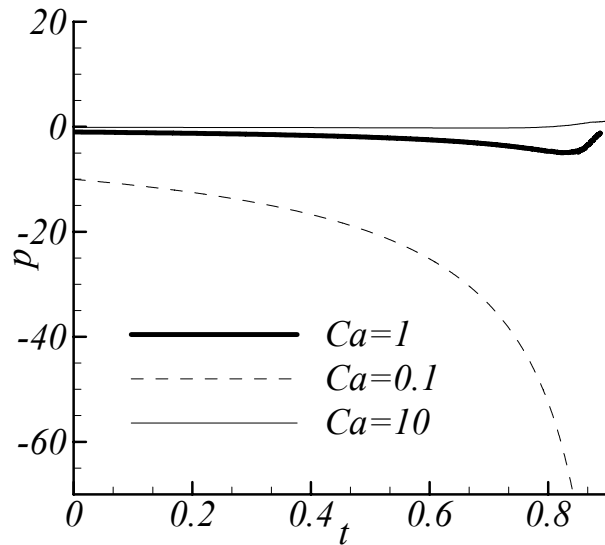
Figure 3.4: Pressure at the center point of the imprint area during imprint for the three Capillary numbers; p is always negative for Ca=0.1, always positive for Ca=10, and transitions from negative to positive for Ca=1.
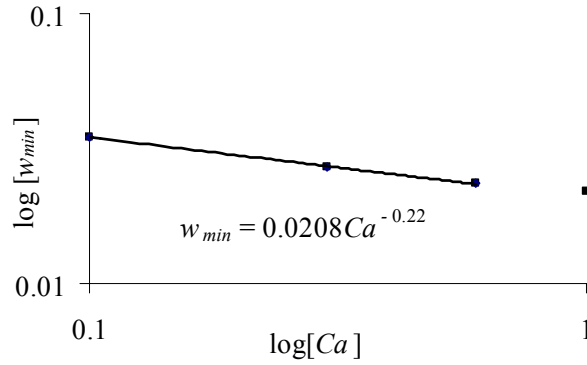
Figure 3.5: The relationship between w_{min} and Ca.

balance $L^2 h_0 = Q$, where Q is the total volume of fluid,

$$Ca^* = \frac{12\mu VQ}{\hat{\gamma}h^3} .$$ (3.21)

Thus, as the gap height becomes smaller the modified capillary number becomes larger, reflecting the larger role of viscous forces that have a greater effect towards the end of the process. The transition from the capillary regime to the viscous regime occurs when the value of Ca^* becomes greater than one. In the case of $Ca=0.1$, Ca^* never reaches a value of one and the transition into a viscous pressure regime does not occur, as demonstrated by the purely negative template deformation. The pressure at the center of the imprint area is plotted over time in Figure 3.4 to demonstrate that large negative pressures for $Ca=0.1$ cause negative deformation whereas positive viscous pressures at the center point for $Ca=10$ create positive deformation by the end of the process. Figure 3.5 shows a plot of the relationship between Ca and the minimum deformation experienced by the template. The trend shown corresponds to roughly $w_{min} \sim Ca^{-1/4}$. Although the scaling analysis prediction from equating the viscous pressure to the

60

capillary pressure predicted $w_{min} \sim Ca^{-1/2}$, the simulation results still shows the slightly downward slope of w_{min} as the capillary number increases as predicted by the scaling. A possible reason for the discrepancy is the assumption in the scaling that the radius of the drop is approximately equal the length of the imprint area, which is not quite the case for the capillary dominant regime where the drop has not spread over the entire imprint area. A plot of w_{max} and its dependence on Ca in Figure 3.6 confirms the scaling $w_{max} \sim Ca$ predicted from viscous pressure scaling arguments.

In dimensional terms, this constant velocity process has a dimensional velocity that is $V = (\hat{\gamma} h_0^2 Ca)/(12\mu L^2)$, which is about 1.45 nm/sec for $Ca=1$, corresponding to a characteristic time $t_c = h_0 / V = 688$ seconds.

The exponential height dependence predicted from these scaling arguments is clearly visible in a plot of w vs. h in Figure 7. The exponential dependence is observed at the end of the simulation (i.e. when h is small, since h is inversely related to t); when h reaches about 30% of its initial value, the viscous pressures create a large positive
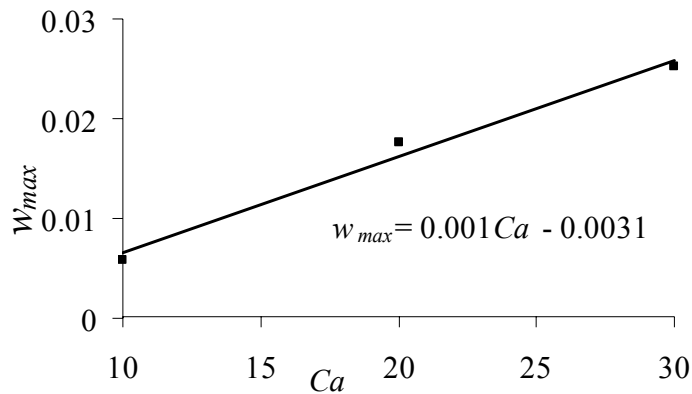
Figure 3.6: The relationship between w_{max} and Ca.
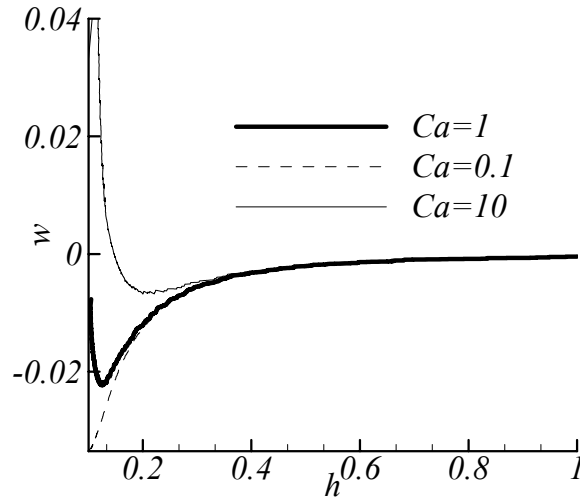
Figure 3.7: Deformation as a function of gap height.

deformation for capillary number ten, and capillary pressures create a large negative

deformation for capillary number 0.1. Equation (3.11) predicts a $1/h$ scaling for w_{min} and

Equation (3.16) predicts a $1/h^6$ scaling for w_{max}; these exponential dependences are

visible from the slow descent of the Ca=0.1 curve that follows w_{min} and the rapid positive

change in w for Ca=1 and 10 curves, for which the w_{max} scaling is relevant.

3.4b. Constant Velocity – Multiple Drops

Constant velocity simulations were performed for a template imprinting arrays of

four and nine drops, placed in a square pattern evenly over the imprint area. Results are

shown in Figure 3.8 for the deformation experienced at Ca=1 for one, four and nine

drops. The trend is that larger numbers of drops create more negative deformation. This

is due to the lack of positive viscous pressure encountered during the imprint for multiple

drops, until the end of the process when the curves all show a trend toward more positive

62

deformations. For the case of one drop, the negative deformation was not as extreme as for four and nine drops due to the balancing viscous pressures that created an upward force on the template during the process, whereas four and nine drops create more negative pressure due to the larger amount of interfacial area where negative capillary pressures exist.

The deformation is instantaneously related to the pressure field, suggesting that at the end of the process, once the drops have merged, the deformations should be the same. As shown in Figure 3.8, exponential increase in deformation at the time when drops merge ($h_{contact}=4h_f/\pi$, where h_f is the final gap height) suggests that the deformation converges to roughly the same positive value by the end of the imprint. The deformation result shown has very low values of deformation due to the simulation of a template with
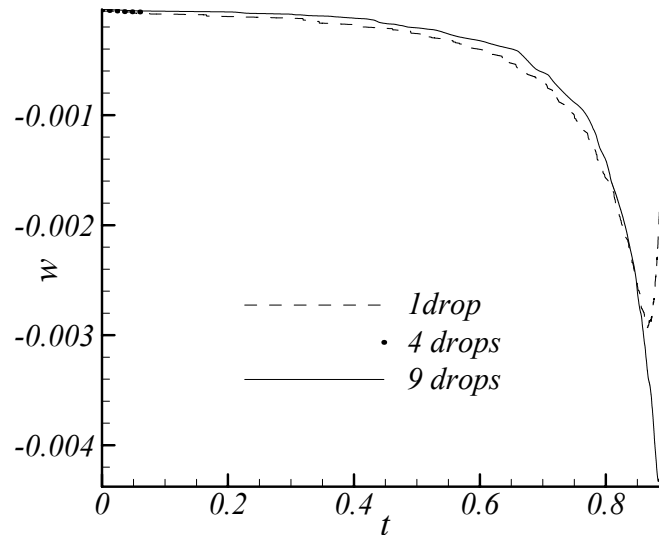
Figure 3.8: Template deformation during the imprint process for a single drop, four and nine drops, all at constant velocity and capillary number of one.

63

thickness twice that shown in other simulation results, in order to obtain more data points on the exponential portion of the curve for better comparison of the single and multiple drop cases. 2D contour plots showing the nature of the concave deformation experienced by a template printing nine drops are shown in Figure 3.9, which includes contour plots of both fluid pressure and template distortion for two points in time during the imprint. Even after the drops have merged there is a net negative capillary pressure on the template due to the strong capillary force at the edge of fluid, causing the negative deformation.
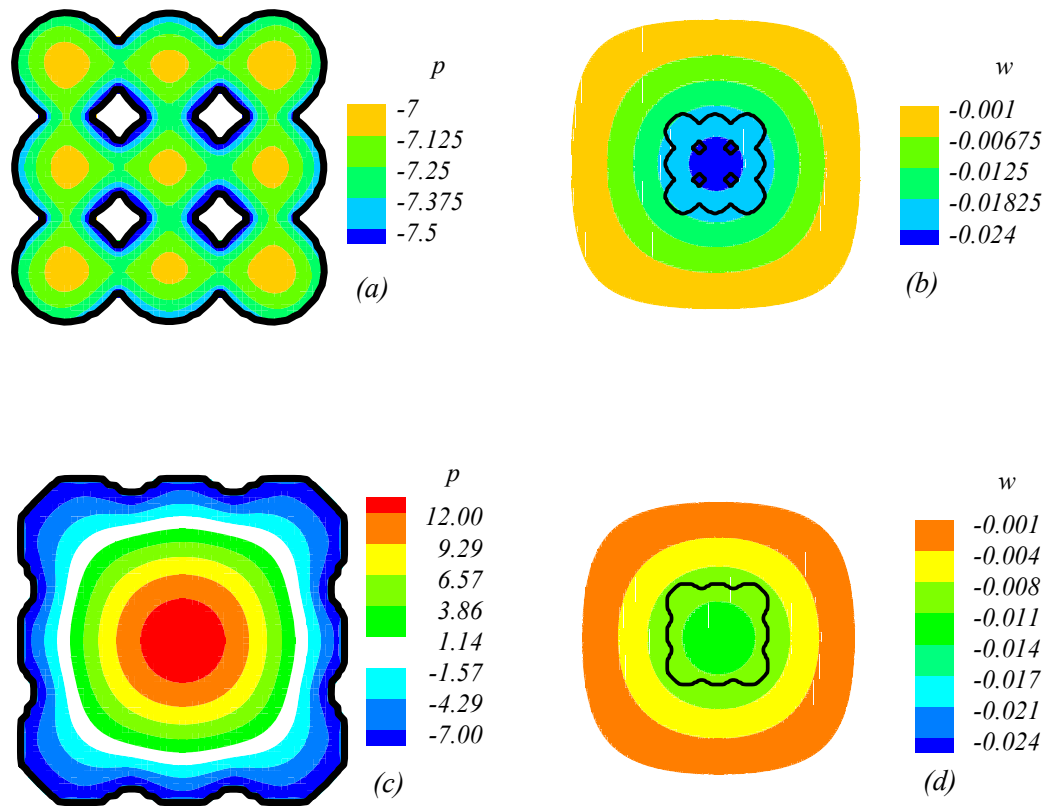
Figure 3.9: Template deformation for nine drops of fluid, black line corresponds to fluid-air interface; (a) t=0.846, higher pressure levels exist in the drop interiors and lower pressure levels exist at drop-air interfaces, both on the outer edge as well as on the interior fluid-air interfaces; (b)t=0.846, negative deformation is shown where the most negative deformation is in the drop center and is zero on the boundary; (c) t=0.86, drops have merged and highest pressure level exists at the center of the imprint area; (d) t=0.86, the deformation is still negative in the center of the imprint area, though more positive than the deformation at t=0.846.

3.4c. Zero Force – Single and Multiple Drops

Simulations were performed for a net force of zero to allow the capillary forces and viscous forces to exactly balance. Figure 3.10 shows the result for w as it changes over time, and there is almost no deformation; since w is nondimensionalized by $h_0=1$ μm, these numbers indicate that deformation would be at most one nanometer. The match between the scaling prediction of $w \sim t^{3/2}$ with the simulation result is very good until the end, where the assumption that the speed of the deformation, i.e. the $\partial w / \partial t$ term in the lubrication equation, is negligible compared to the plate velocity V is no longer valid. The deformation tapers off due to the slowing of the plate at the end of the imprint,
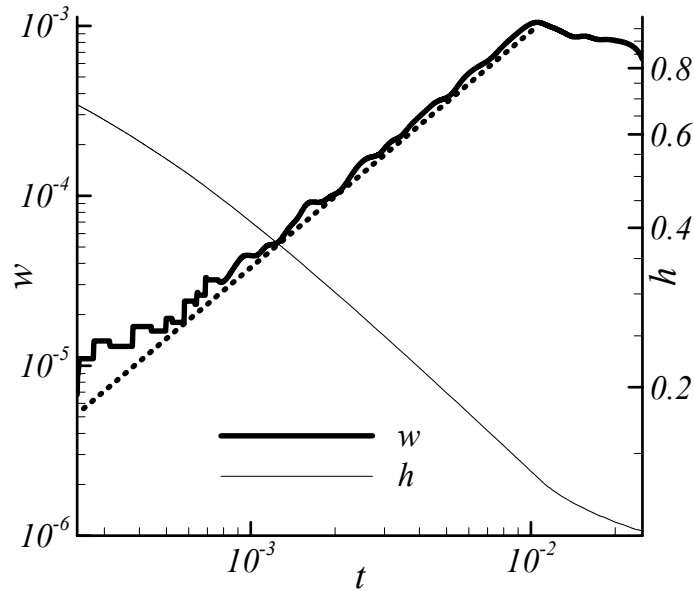
Figure 3.10: Template deformation during a zero force process for one drop. Dotted line represents a slope of -3/2, followed very closely by simulation results.

where higher viscous forces cause the plates velocity to slow in order to maintain the zero force condition.

Results for multiple drop simulations indicate the same negligible deformation. Imprint time is improved with the use of more drops, as reported in previous work [5], where the gap height over time for varying number of drops N was given:

$$h = \left[1 + 16\pi N \left(\frac{h_0}{h_f} \right) t \right]^{-\frac{1}{2}} . \tag{3.22}$$

This scaling is included as dotted lines for one, four and nine drops in Figure 3.11. The scaling and computation are closely matched, except at the end where the rate of template motion slows due to the need to fill the corners of the imprint area. It is clear that including the effects of template deformation does not undermine this improvement in
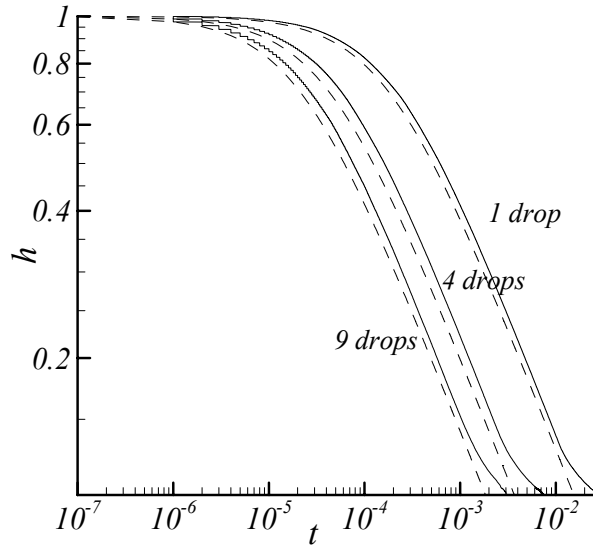
Figure 3.11: Gap height during a zero force process for one, four and nine drops. Dotted lines represent scaling predictions.

imprint time for increasing numbers of drops. The characteristic time for a zero force

process is $t_c = \dfrac{12\mu L^2}{\hat{\gamma}h}$ =688 seconds, so for a single drop the time for imprinting a 100 nm

base layer is about 20 seconds, whereas for nine drops it is just 2.5 seconds. This order

of magnitude improvement for using multiple drops is a great advantage in the zero force

process.

3.5. Conclusions

A coupled fluid-solid dynamics simulation of drops moving under varied template

motion schemes at different capillary number conditions has been presented. The

severity of template deformation depends greatly on the capillary number at which the

imprinting takes place. In the case of a template moving at constant velocity and a large

capillary number ($Ca>1$), viscous forces cause positive deformations in the center of the

plate, and if the capillary is small ($Ca<1$), capillary forces will cause large negative

deformations in the center of the plate. Use of multiple drops actually makes the negative

deformation during the imprint slightly more significant than for a single drop, with final

positive deformation roughly the same as for a single drop. It is therefore not necessarily

advantageous to use multiple drops if the template control scheme is a constant velocity

motion, so that imprint time is fixed, and the capillary number is $O(1)$. If, however, the

capillary number for the system is large, $O(10)$ or greater, due to a more viscous or lower

surface tension monomer, multiple drops may be useful to avoid positive deformations

during the imprint process, though final deformations at the end of the process will

undoubtedly be very large at such a large capillary number.

The more elaborate but certainly more effective method for controlling deformation is to implement a zero force scheme for the moving template, where capillary forces suck the template toward the substrate so that capillary forces and viscous forces exactly balance. This not only creates negligible amounts of template deformation but is also advantageous for its shorter imprint time, which can be made even shorter with the use of multiple drops. This study has shown the importance of the template control scheme in limiting template deformation as well as explored the interesting effects of capillary number on the way the template can deform in a concave or convex manner, for either small or large capillary number.

3.6 References

[1] T.C. Bailey, S. C. Johnson, S. V. Sreenivasan, J.G. Ekerdt, C.G. Willson, D.J. Resnick, J. Photopolymer Sci. Tech. 15 (3) (2002) 481-486.

[2] J. Haisma, M. Verheijen, K. Van den Heuvel, J. Vac. Sci. Technol. B. 14 (1996) 4124-4129.

[3] T. C. Bailey, S.C. Johnson, M.D. Dickey, J.J. Smith, A.T. Jamieson, E.K. Kim, N.A. Stacey, D. Mancini, W.J. Dauksher, K. Nordquist, D.J. Resnick, S.V. Sreenivasan, J.G. Ekerdt, C.G. Willson, in: Proceedings of the 39th Interface Symposium, 2002.

[4] S. Reddy. R.T. Bonnecaze, Microelectronic Engineering 81 (2005) 60-70.

[5] S.D. Schuetter, G. A. Dicks, G. F. Nellis, R. L. Engelstad, E. G. Lovell, J. Vac. Sci. Technol. B 22 (6) (2004) 3312-3317.

[6] E. Ventsel, "Thin Plates and Shells: Theory, Analysis and Applications" New York (2001).

[7] C.W. Hirt, B.D. Nichols, J. Comp. Phys. 39 (1981) 201–225.

Chapter 4: The Dynamics of Low Capillary Number Interfaces Moving Through Sharp Features

4.1. Introduction

The Step and Flash Imprint Lithography (SFIL) process offers a high-throughput, low-cost alternative to modern methods of lithography. The process makes use of the liquid monomer form of the etch barrier. The monomer drops, which are typically acrylate based formulations, are pressed into the desired shape by bringing a template, typically a quartz mask, down with a given speed or applied force, making best use of the capillary and viscous force interaction to minimize the imprint time [1]. The imprint area is one square inch with a final base layer of approximately 50 nm; the template velocity begins on the order of a micron per second and drops to just a few nanometers per second at the end of the process. The SFIL technique has allowed production of features as small as 30 nm, after imprint and etch [2]. Typical capillary numbers for these flows are very small due to the small feature size and relatively low flow rates. Given a monomer with typical density $O(1 \text{ g cm}^{-3})$, interfacial tension $O(30 \text{ dyne cm}^{-1})$, and viscosity $O(1 \text{ cP})$, the capillary number is as small as 10^{-3}. The Reynolds number is, at the largest, on the order of 10^{-3}.

Clearly, capillary wetting is an important part of the filling process, and is particularly important for filling of features in the template. If features do not fill appropriately, instead trapping an air bubble inside, the resulting photoresist image is untrue to the original mask and the failed pattern transfer can lead to a non-functional

circuit on the wafer. A fundamental understanding of this nano-scale filling process is useful for predicting which types of features will fill or trap air; the goal of this study is to obtain this fundamental understanding through simulation of the interface movement through the template features.

Feature filling applications in other processes, such as injection molding, encounter similar flow effects at feature edges. Numerical techniques have been developed to handle the effect of the vertical fluid movement at sharp corners such as T-junctions [3]. Studies have also been done on the motion of an advancing interface [4]. These are generally high capillary number flows, unlike those in imprint lithography [5]. Little is known, however, about low-capillary number interface motion through these sharp lithographic features.

4.2. Model

Consider the following two-dimensional feature filling illustrated schematically in Figure 4.1. A Newtonian fluid of viscosity μ and density ρ is injected from the left inlet
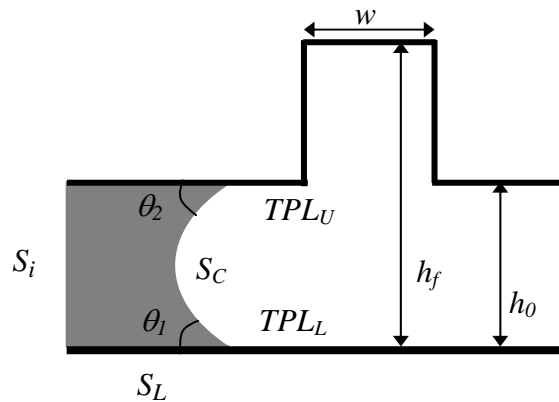
Figure 4.1: Schematic of an individual feature. The simulation begins with a small amount of fluid in the region before the feature, with boundaries S_i, S_C, S_u, and S_L, as well as contact lines TPL_U and TPL_L positioned at the three phase lines. The feature is of height h_f and width w, and the gap is of height h_0.

S_i at a constant average velocity U in the gap between a lower flat surface S_L and an upper

surface S_U that has a rectangular feature. The gap has a nominal height h_0, and the height

and width of the feature are h_f and w, respectively. The static contact angles at the lower

and upper contact lines (three-phase lines TPL_U and TPL_L) are θ_1 and θ_2. The sharp

corners of the feature are modeled using rounded corners with very small radii of

curvature equal to 1% of the gap height. This allows the computation to progress

smoothly, avoiding numerical instability at the corners.

Although in practice the nanoimprint process has the upper surface move towards

the lower surface to close the gap, it is a convenient approximation to simulate the

process by allowing fluid to move into the cavity, while keeping the surfaces at a constant

gap height. This is valid due to the comparative magnitudes of the horizontal (inlet) and

vertical template velocities, U and V, where the horizontal velocity scales as $U \sim (R/h_0)V$,

where R is the radius of the drops and is much greater than h_0. Thus, $U >> V$ and the

change in the gap height and vertical velocity can safely be neglected during the feature

filling process.

The flow is described by the dimensionless Navier Stokes equations of motion,

$$\nabla \cdot \mathbf{v} = 0 \qquad (4.1)$$

$$Re\left(\frac{\partial \mathbf{v}}{\partial t} + \mathbf{v} \cdot \nabla \mathbf{v}\right) = -\nabla p + \nabla^2 \mathbf{v}, \qquad (4.2)$$

where $Re = \rho \gamma h_0/\mu^2$ is the Reynolds number, ρ is the fluid density, γ is the surface tension,

$\mathbf{v}$ is the fluid velocity, t is time, μ is the fluid viscosity, and p is the fluid pressure. The

pressure, velocity, and lengths have been non-dimensionalized by γ/h_0, γ/μ, and h_0

respectively. Due to the scale of this process the inertia of the flow is generally negligible with $Re \approx 10^{-4}$, for typical parameters $h_0 = 100$ nm, $\mu = 1$ cP, $\gamma = 30$ dyne cm^{-1}, and $\rho = 1$ g cm^{-3}.

At the inlet S_i, fluid is injected at a constant rate so that,

$$-\mathbf{n} \cdot \mathbf{v} = Ca = \frac{\mu U}{\gamma}, \tag{4.3}$$

where $\mathbf{n}$ is the outwardly directed surface normal and Ca is the Capillary number in its common form, as opposed to the form given in Chapter 2 Equation (2.7), which was relevant in the lubrication scaling discussed in Chapter 2. As defined in Equation (4.3), the Capillary number is typically on the order of 10^{-3}. The magnitude of capillary force is much more significant than the magnitude of van der Waals force. The capillary pressure can be expressed as $P_{capillary} = -\gamma / h$, where h is the channel height and at smallest is 10nm. The van der Waals pressure can be expressed as $P_{VDW} = A_H/(6\pi h^3)$, where A_H is the Hamaker constant for the material (-1.7×10^{-20} is a typical value for PMMA on Silicon). The ratio of these pressures is $P_{capillary} / P_{VDW} = 2.5 \times 10^3$, validating the dominance of capillary forces in this process and allowing us to neglect the effect of van der Waals forces.

In addition to the condition of no flow through the upper and lower surfaces S_U and S_L $(\mathbf{n} \cdot \mathbf{v} = 0)$, there are also partial slip boundary conditions given by

$$\mathbf{t} \cdot \left[\mathbf{v} - \mathbf{v_s} \exp(-\alpha r) \right] = 0, \tag{4.4}$$

where $\mathbf{t}$ is the tangent vector on the surface, α is the decay parameter or roughly the inverse slip length, $\mathbf{v_s}$ is the velocity of the interface and r is the distance from the contact

line. A very small slip length, with $\alpha = 10^{-3}$, was used for S_L. A longer slip length, with α $= 10^{-2}$, was enforced on S_U due to its discontinuous nature.   These slip lengths corresponded to roughly one mesh element over S_L and five mesh elements over S_U, due to the irregular FEM grid used over the fluid domain. Simulations with much finer mesh elements showed similar behavior, so the results are independent of the size of the grid elements.

At the fluid-vapor interface S_C the kinematic and normal stress conditions are applied, as given by

$$\mathbf{n}\cdot(\mathbf{v}-\mathbf{v}_S)=0, \tag{4.5}$$

and

$$p = \nabla\cdot\mathbf{n}+\mathbf{n}\cdot\left(\nabla\mathbf{v}+\nabla\mathbf{v}^T\right)\cdot\mathbf{n}. \tag{4.6}$$

The points at the upper and lower three-phase-lines, TPL_U and TPL_L, both carry contact angle boundary conditions on the mesh equations, where the contact angle is defined as the angle between the wall and the free surface normal.

$$\mathbf{n}\cdot\mathbf{n}_w = \cos\theta \tag{4.7}$$

where $\mathbf{n}_w$ is the wall normal. For the full numerical simulations, both contact angles are set to 30°.

This rigid contact angle constraint may be replaced by a dynamic contact angle boundary condition, in which the contact angle may be determined by the following expression from molecular-kinetic theory [6]:

$$v = \frac{2\kappa_S^0 h\lambda}{\mu\upsilon_L}\sinh\left[\frac{\gamma}{2nk_BT}\left(\cos\theta_0 - \cos\theta\right)\right] \tag{4.8}$$

75

where v is the wetting line speed, h is Planck's constant, μ is the liquid viscosity, v_L is the unit of flow for the liquid (generally the molecular volume), γ is the surface tension of the liquid, k_B is Boltzmann's constant, T is absolute temperature, n is the number of adsorption sites per unit area, $\lambda = 1/\sqrt{n}$, θ_0 is the equilibrium (static) contact angle, θ is the dynamic advancing contact angle, and κ_s^0 is given by

$$\kappa_S^0 = \frac{k_B T}{h} \exp\left(\frac{-\Delta g^*}{n k_B T}\right),$$ (4.9)

where Δg_s^* is the surface contribution to the specific activation free energy of wetting. Using typical values of a liquid monomer, with $v_L = O(10^{-10})$, and $n = O(10^{18})$, the prefactor $\gamma/(2 n k_B T)$ is $O(1)$ and when multiplied by $(\cos\theta_0 - \cos\theta)$, the sinh argument is $O(10^{-1})$, so that we can replace Equation (8) with a simplified, linearized version of the dynamic contact angle model,

$$v = U v_0 (\cos\theta_0 - \cos\theta),$$ (4.10)

where v_0 is a dimensionless constant,

$$v_0 = \frac{2\kappa_S^0 h \lambda}{\mu v_L} \frac{\gamma}{2 n k_B T} \frac{1}{U},$$ (4.11)

and $v_0 = O(10^{-1})$, computed from typical values given above and $\Delta g_s^* = 86$ mJ/m^2 (from Blake and De Coninck[6]), $U = 10^{-2}$ (the capillary motion horizontal velocity), and an equilibrium contact angle of $\theta_0 = 28°$, for a monomer that is wetting to the surface.

The simulations were performed using a software package known as *Goma*, which is ideal for simulating processes in which the bulk fluid transport is closely coupled to the interfacial physics. *Goma* is a two- and three-dimensional finite element

program that has been demonstrated to accurately model free or moving interfaces [7,8,9,10]. It includes a full Newton coupled heat, mass, momentum, and pseudo-solid mesh motion algorithm for solution of the conservation equations using the Galerkin method of weighted residuals on a fully-coupled Newton-Raphson iterative scheme. The code uses a moving mesh algorithm that treats the domain as a computational Lagrangian solid that deforms based on the physics of the problem. The computational time to move the interface by frames shown in the results section, Figure 4.2, varied from 1 to 3 days depending on the number of re-mesh steps required; the interface stretching required re-mesh steps roughly every 50 time steps. The simulations were performed on a Compaq machine with clockspeed 2.4 GHz and 2Gb RAM. Due to the long amount of processing time and problems with mesh distortion, this software was only useful for the detailed feature filling simulations and was not considered for comparison with the lubrication simulation presented in Chapters 2 and 3.

4.3. Results and Analysis

Figure 4.2 displays a typical timetrace of the fluid-air interface as it moves through a feature under low Capillary number conditions, where $Ca=10^{-3}$. The interface initially takes on a circular arc shape by $t=5.9$ (dimensionless units), until reaching the feature corner where it effectively pins to the inner corner of the feature, at $t=757$, as the upper contact line negotiates around the feature corner while the bottom contact line moves along the wafer surface. The upper contact line then moves vertically to the top corner of the feature, by $t=1852$, at which point the highly stretched interface is able to reconfigure into a stable lower surface energy conformation at $t=1876$. This reconfiguration involves a rapidly advancing upper contact line in concert with a rapidly receding lower contact line to bring the interface into a more stable, lower surface energy position. Finally the interface moves through the final corner of the feature and fills by $t=2633$. It is important to note the time scale of the reconfiguration process, which happens more than an order of magnitude faster than any other event in the filling
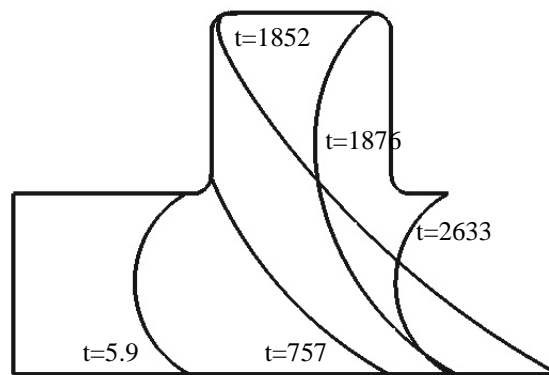
Figure 4.2: Timetrace of the interface motion through a feature at $Ca=10^{-3}$. Times are denoted for each interfacial position shown.

78

process.

In order to confirm that this interface reconfiguration is not an artifact of enforcing the contact angles to be 30 degrees, the contact angle boundary condition was modified to allow flexibility in the contact angle condition using the dynamic contact angle theory described in the simulation section. This simulation was also performed at an order of magnitude higher capillary number, $Ca=10^{-2}$. The results are shown in Figure 4.3, where it can be seen that the entire filling process is an order of magnitude shorter in time, due to the higher capillary number. Even at higher capillary number flow with a dynamic contact angle, the interface reconfiguration is roughly an order of magnitude faster in time than any other event in the filling process.

On closer inspection of Figure 4.3, it is apparent that the interface stretches to a point where it nearly touches the far corner of the feature. If the interface were to move through a feature whose geometry was such that the interface did indeed catch on the far corner, as depicted in Figure 4.4, the feature may trap an air pocket and thus not fill
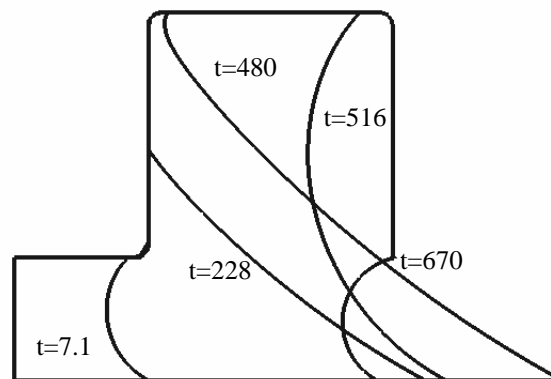
Figure 4.3: Timetrace of the interface motion for a simulation using dynamic contact angles on the upper surface and at $Ca=10^{-2}$. Times are denoted for each interfacial position shown.

79
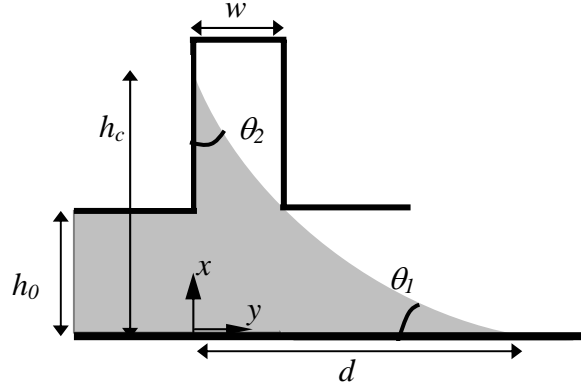
Figure 4.4: A stretched interface configuration
that catches the far corner of the feature.

appropriately. Simulations were performed for various geometric conditions, using the constrained contact angle condition and low capillary number wetting. The results, shown as large and small circles corresponding to features that filled or trapped air due to interface stretching, are shown in Figure 4.5. There is a clear trend for air trapping as either the aspect ratio becomes high or the feature becomes relatively narrow.

It is possible to solve the interface entrapment geometrically, assuming the interface is a circular arc and the contact angles are known. The set of equations to be solved for such a geometric analysis include:

$$(w - x_0)^2 + (h_0 - y_0)^2 = r^2, \tag{4.12}$$

$$(-x_0)^2 + (h_c - y_0)^2 = r^2, \tag{4.13}$$

$$(d - x_0)^2 + (-y_0)^2 = r^2, \tag{4.14}$$

$$r = \frac{h_c}{\cos\left(\theta_2 + \dfrac{\pi}{2}\right) + \cos(\theta_1)}, \tag{4.15}$$

80

$$h_c = d \tan\left(\frac{\theta_1 - \theta_2 - \pi/2}{2}\right),$$

(4.16)

where x_0 and y_0 are the coordinates of the center of the circle that the circular arc interface belongs to, r is the radius of that circle, w is the feature width, d is the horizontal length of stretched interface, h_0 is the initial gap height, h_c is the critical height to which the upper contact line must rise for the interface to touch the far corner of the feature, and θ_1 and θ_2 are the contact angles. The boundary delimiting the fill and no fill regions is shown by the dashed line in Figure 4.5, which is the exact numeric solution to these equations. An analytic asymptotic solution, for $\theta_1 \ll \pi/2$ and $\theta_2 \ll \pi/2$, can also be expressed in terms of the geometric parameters and is given by
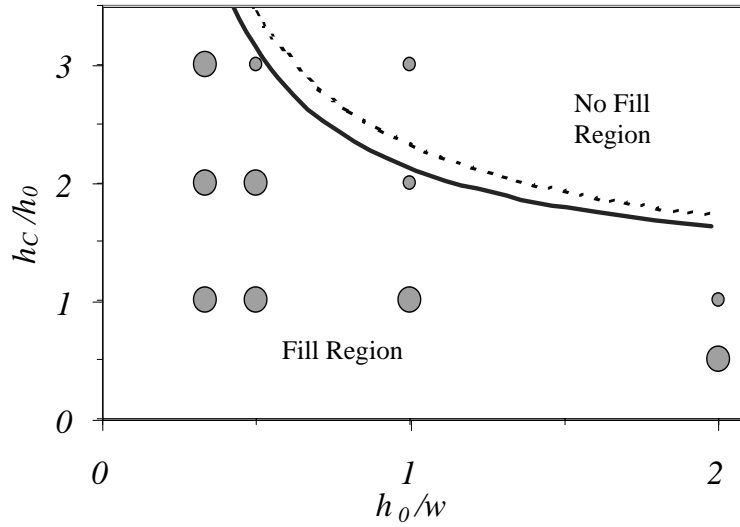
Figure 4.5: Result for the Goma simulations, filled features (large circles) and unfilled features (small circles); curves show results for geometry analysis, both the exact numeric solution (dashed line) and the asymptotic solution given by Equation (4.17) (solid line).
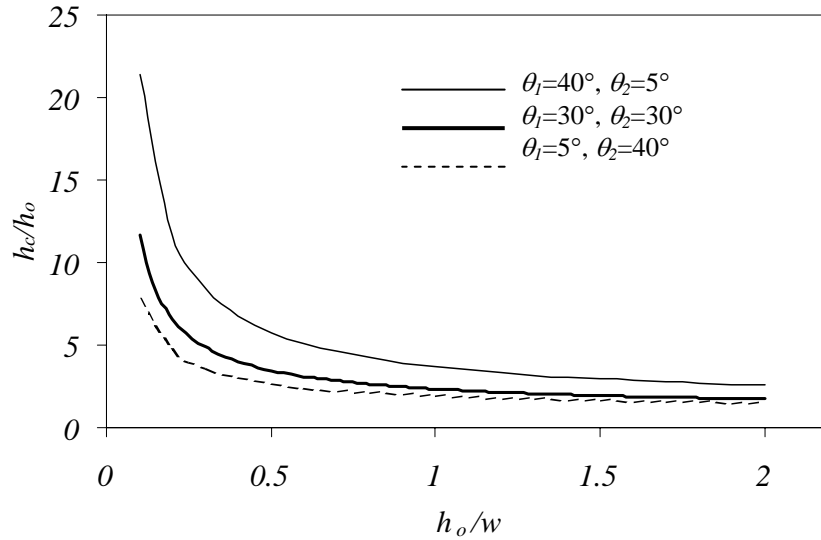
Figure 4.6: Geometry study based on the assumption of a circular arc shaped interface, with wetting contact angles on both surfaces.

$$w \cong 2h_c \left[1 - \left(\frac{h_0}{h_c} \right)^{\frac{1}{2}} \right] \tan(\theta_2) + O(\tan^2(\theta_1)) . \tag{4.17}$$

The prediction of the approximate model is shown by the solid line in Figure 4.5, and it follows the exact geometric model closely. Geometric results are also shown for a range of wetting contact angles in Figure 4.6. Since the area under the curves is largest for the case where the substrate is less wetting than the template, this is the case that is most advantageous for feature filling. This is due to the interface stretching occurring more significantly in the vertical direction rather than the horizontal direction, so that the interface is less likely to catch on the far corner of the feature when the upper contact angle is more wetting than the lower contact angle.

4.4. Discussion

The feature filling process for low capillary number fill is clearly depicted here as an interface driven process, where fast interface reconfiguration pushes the fluid into the feature and allows it to fill. The rapid reconfiguration of the interface is the key step in the overall filling process; once this occurs, the remainder of the feature fills at the same timescale as the surrounding area. This rapid reconfiguration is due to the unstable nature of the stretched interface, which is brought to an equilibrium position by taking on a lower surface area conformation inside the feature. The interface instability occurs when the upper contact line rounds the top inner corner. At this point, the extreme curvature of the interface near the upper contact line drives fluid near the interface toward the top corner, effectively pulling the lower contact line back to allow the interface to take on a more stable configuration.

The filling process includes a stretching of the interface as the upper contact line pins to the inner corner of the feature. This stretched interface configuration can lead to air entrapment in features. Features large in width or of low aspect ratio are much easier to fill than narrow features for any given aspect ratio, but below an aspect ratio of about unity, features will generally fill with ease. A geometric study gives a very good prediction on how this stretched configuration will affect feature filling for a given aspect ratio and feature width. The geometry study also shows that for a substrate that is less wetting than the template, a wider variety of features will fill. A variety of contact angles was also explored in the simulations of the interface motion, where contact angles varied from 5 to 40 degrees, and the phenomena of the rapid interface reconfigurations was

found to be similar in these cases, though the filling of features varied based on feature dimensions.

Results for rapid interface reconfiguration have been seen experimentally in the study of foam lamella movement through porous media [11]. An enforced pressure gradient through a pore causes a lamella to move forward through the pore. As the lamella moves through the widest part of the pore, analogous to the corner of the feature, it rapidly snaps forward into the narrow portion of the pore. This movement from a highly stretched, high surface energy conformation to a low energy, equilibrium surface conformation is very similar to the interface reconfiguration predicted in the simulations in this study.

The understanding gained from these simulations is usefully implemented in a 2D simulation of the imprint process of the fluid movement over the wafer area, i.e. the plane perpendicular to the profile view considered in this study. The plan view may be modeled using the lubrication approximation and capillary boundary conditions on the pressure[1]. Though the details of the vertical fluid-air interface movement cannot be captured in this plane, the pressure field and the reconfiguration around sharp corners relevant to the lubrication model may be captured by an effective *ad hoc* boundary condition. The premise is to allow the pressure to buildup at the interface when it arrives at the feature corner until the pressure is large enough to match the necessary interfacial pressure for the interface to exist inside the feature cavity at equilibrium. This pressure buildup is simply used to mock the pressure at the interface near a feature and the effects of interfacial reconfiguration that is taking place in the vertical dimension. Thus, the

macroscopic boundary condition, in which the interface reconfiguration is represented by a pressure buildup at the interface, progresses from the initial capillary pressure to an intermediate pressure, until it reaches the final heightened pressure inside the feature;

$$p_{initial} = -\frac{\gamma}{h_{small}},$$ (4.18)

$$\mathbf{n} \cdot \nabla p_{intermediate} = 0,$$ (4.19)

$$p_{final} = -\frac{\gamma}{h_{l\arg e}},$$ (4.20)

where $p_{initial}$ is the boundary pressure of the interface at the entrance to the feature, h_{small} is the height of the gap outside the feature, $p_{intermediate}$ is the boundary pressure during the interface stretching, p_{final} is the boundary pressure of the interface inside the feature, and h_{large} is the height of the gap inside the feature. By solving the lubrication equation for the intermediate pressure, the pressure at the interface is allowed build without actually moving the interface until the pressure reaches p_{final}. This effective boundary condition is similar in spirit to the Haines critical curvature for imbibition of a wetting phase into a porous medium [12].

4.5. Conclusions

This study provides insight on the motion of the fluid-air interface through sharp features at low-capillary number. The rapid interface reconfiguration may be simulated in detail in the profile plane of the gap between the upper and lower surfaces, going through a stretched configuration as the upper contact line effectively pins to the initial feature corner, and then quickly reconfiguring into a more stable conformation inside the feature as soon as the upper contact line advances through the upper feature corner. This

detailed motion cannot be captured in the macroscopic simulation of the 2D fluid flow over the area of the substrate, but the overall effect of the interface stretching and reconfiguration at the feature edges can be encapsulated in an effective macroscopic boundary condition. Through this effective boundary condition, the process may be modeled as a pressure buildup at the interface when it encounters a feature's edge; this buildup continues until the interface has obtained the pressure it must achieve to exist inside the feature at equilibrium, *i.e.* reconfigured to exist inside the feature.

4.6. References

[1] S. Reddy, R. T. Bonnecaze, Microelectron. Eng. 82 (1) (2005) 60-70.

[2] D. J. Resnick, D. Mancinia, W. J. Daukshera, K. Nordquist, T. C. Bailey, S. Johnson, S. V. Sreenivasan, J. G. Ekerdt, C. G. Willson, Microelectron. Eng. 69 (2003) 412-.

[3] G. Batch, International Polymer Processing 12 (1997) 257.

[4] D. Fauchon, H. H. Dannelongue, P. A. Tanguy, International Polymer Processing, 6 (1991) 13.

[5] H. Mavridis, A.N. Hrymak, J. Vlachopoulos, AICHE Journal 34 (1988) 403.

[6] T. D. Blake, J. De Coninck, Advances in Colloid and Interface Science 96 (2002) 21.

[7] P. A. Sackinger, P. R. Schunk, R. R. Rao, J. Comp. Phys. 125, 83 (1996).

[8] H. Fan, Y. Lu, A. Stump, S. T. Reed, T. Baer, P. R. Schunk, V. Luna, G. Lopez, C. J. Brinker, Letters to Nature 405 (2000) 56.

[9] R. A. Cairncross, P. R. Schunk, T. Baer, R. R. Rao, P. A. Sackinger, Int. J. Numer. Meth. Fluids 33 (2000) 375.

[10] T. Baer, P. R. Schunk, R. A. Cairncross, R. R. Rao, P. A. Sackinger, Int. J. Numer. Meth. Fluids 33, (2000) 405.

[11]W.R. Rossen, J. Colloid and Interface Science 136 (1) (1990) 38-53.

[12] W.B. Haines, J. Agric. Sci. 17 (1927).

Chapter 5: Summary and Conclusions

The ability of the SFIL process to break through as a high-throughput and low-cost fabrication method for industrial scale chip manufacturing depends significantly on the fluid issues presented in this study. The SFIL technique offers promising aspects that circumvent the need for high cost optics systems that suffer from resolution problems; it must, however, produce high fidelity imprints at nanoscale resolution in a fast step-and-repeat process. Thus I have undertaken this computational study of the physics of the fluid behavior during the imprint process to provide the ability to understand and manipulate issues such as imprint pressure, imprint time, template distortion and feature filling.

5.1. Simulation

Initial understanding of the fluid issues has been achieved via simulation of the equations of motion using the simplifying assumption of lubrication theory. This theory has been implemented in a computational simulation of the fluid pressure using a choice of iterative solvers and matrix preconditioners from a linear algebra library.

The Volume of Fluid method is used to evolve the interface position over time as multiple drops merge to fill the imprint area, producing a dynamic simulation of the fluid flow over the imprint area until the final base layer is achieved. Using a boundary condition on the pressure field that incorporates the capillary force at the fluid-air interface, the interplay of viscous and capillary forces can be modeled over the course of the imprint.

Incorporation of the solid mechanics of elastic deformation of the template was achieved using thin plate theory. The solid mechanics and fluid mechanics are coupled due to the dependence of the thin plate equation on the fluid pressure and the dependence of the lubrication equation on the gap height (which is dependent on the amount of solid deformation). The solution of this coupled system was achieved using an iterative scheme where the lubrication equation and thin plate equation were solved using the solution from one as input to the other until the solutions for the deformation field and pressure field converged. After convergence of the solution, the fluid interface was advanced and the system was solved again at the next time step. This procedure enabled a dynamic simulation of the fluid motion and solid deformation over the course of the imprint.

Simulation of the feature filling was performed in both the lateral and vertical dimensions. The lateral motion of the fluid-air interface was simulated using the lubrication code with a modified boundary condition that incorporated the physics of a pressure jump required for feature filling. The nature of feature filling in the vertical direction was simulated by solution of the equations of motion, using a software package that could couple the bulk fluid transport to the interfacial physics. This software was modified to handle a variable wall normal for the contact line motion around feature corners. Boundary conditions on the top and bottom surfaces were no-slip but at the contact points a small region of slip was allowed in order to model the moving contact line phenomena.

5.2. Template Control Schemes

It was found that imprint pressure may best be controlled using a net zero force scheme as opposed to a constant velocity or applied force scheme. In a zero force template control scheme, the capillary forces suck the template toward the wafer so that the negative capillary force is exactly balanced by the positive viscous force, thus exerting a net zero force on the template. In this case, the overall imprint pressure is so low that almost no template deformation occurs. Although an applied force or constant velocity scheme for the moving template may reduce imprint time, it also increases fluid pressures, causing significant deformations in the template. Interestingly, a constant velocity scheme may actually cause negative deformation in the template, where the middle of the template bows toward the substrate due to the sucking force of the negative capillary pressure.

A zero force regulation for template motion relies on capillary force to pull the plates together. As the imprint approaches the final base layer, the viscous forces in the center of the imprint area take on very large positive values due to the thin gap width, but for the same reason the capillary forces become very negative at the fluid-air interface due to the inverse relationship between capillary pressure and gap height, so the balance between the forces continues until the end. Using multiple drops creates a larger amount of fluid-air interface, thus increasing the negative capillary force that essentially sucks the template toward the wafer more quickly, resulting in shorter imprint time. When the drops merge as the base layer approaches its final height, the rate of imprint slows as the fluid area essentially becomes one large drop; however, even with this slowing of the

template speed, the imprint time is faster with multiple drops. In fact, for many drops (~50) the imprint time becomes comparable to applying a 50N force to the template for a single drop. This decrease in imprint time for use of multiple drops is true for either a rigid or deformable template.

5.3 Feature Filling

The fidelity of pattern transfer from the template to the substrate depends upon the complete filling of all features in the template. The filling of these features has been presented in both planes of motion, the plan view afforded by the lubrication simulation showing the way features fill laterally, and the profile view providing information on the fluid-air interface motion based on the motion of the upper and lower contact lines moving over the template and substrate respectively.

The detailed understanding of the fluid-air interface reconfiguration was obtained by performing a full simulation of the fluid-air interface in the profile view under low capillary number conditions using no simplifying assumptions. This simulation provided new insight into the mechanics of the interface motion as the top contact line negotiated its way over the feature corners. The top contact line was found to be effectively pinned to the initial feature corner while the bottom contact line continued to move along the substrate surface, creating a stretched interface conformation. As the top contact line moved up the inner wall of the feature cavity, the interface continued to stretch. When the top contact line finally moved through the first inner corner of the feature cavity, the interface rapidly reconfigured into a more stable conformation with lower surface area,

causing the bottom contact line to quickly recede into a position directly under the top contact line.

This rapid interface reconfiguration happens extremely quickly, as a non-equilibrium process, and is, therefore, best incorporated in the macroscopic lubrication code as an effective pressure-buildup before fluid enters a feature. A geometry study was employed to compare with results from the simulations to predict the ability of features to fill, and both results demonstrated that narrow or high aspect ratio features are much less likely to fill correctly, *i.e.* trap air due to the stretched interface catching the far corner of the feature cavity, than wide or low aspect ratio features. This new insight into a phenomenon poorly understood previously could be a useful tool in understanding which features will fill for given conditions.

Simulation of feature filling in the plan view using lubrication theory required incorporation of the pressure jump required for the interface to enter a feature cavity. Although the details of the vertical motion of the contact line up the feature wall could not be incorporated into the lubrication model, a modified boundary condition was constructed to mimic the pressure buildup that the fluid must go through to enter the feature. Results from this simulation displayed the lag time that the interface would undergo in order to fill a feature while fluid around the feature continued to advance. The amount of lag time before the pressure buildup becomes enough to push the interface into the feature depends on the aspect ratio of the feature. It was found that higher aspect ratio features take more time to fill and may not fill at all due to this time lag. This "macroscopic" understanding of feature filling was possible through the detailed

"microscopic" knowledge obtained from the profile view simulations of the fluid-air interface reconfiguration.

In order to gain some insight into imprint pressures for densely packed features, such a specific model would not be useful. Instead, computations were done using the lubrication code to model fluid flow over a template with a step function in its height, where a portion of the template-substrate gap would have double the final volume of the other portion. The high volume area mimics an area on a template with many feature cavities that need to be filled, while the low volume area corresponds to a flat area or low feature density area on the template. This model showed that dispense of equal volume drops leads to extremely high pressures in the low volume area and increased imprint time compared to a situation where drop volumes are weighted corresponding to their position in the imprint area; if drops in the high volume region are given twice the volume as drops in the low volume region, the imprint pressures are relatively low and the imprint time is much faster.

5.4. Conclusions and Future Work

The interplay between viscous forces and capillary forces is extremely important to all fluid issues. Understanding of the relationship between these forces and how they are best controlled via different template motion schemes is extremely important for the efficiency of the SFIL process. Maintaining a balance of the viscous and capillary forces so that the process runs at a net zero force proves particularly useful if template deformation is a concern, since it limits deformation to negligible values. In order to speed up this process, multiple drops may be used to generate more capillary pressure

with the power to suck the template to the substrate faster, thus shortening the imprint time. For a template with a high density of features in a particular region and a low feature density or flat region, viscous pressure can build to significant levels if drop volume is not correctly apportioned. These large viscous forces can slow the imprint time and cause deformation in the template, proving the importance of strategic drop placement with appropriate drop volume.

Understanding of the details of interface motion also involves careful consideration of the capillary and viscous forces, both in the lateral and vertical directions. Study of the lateral fluid motion showed that a lag time exists due to the need for viscous pressures to build up and push the interface into a higher capillary pressure (*i.e.* less negative) region inside the feature cavity. Once this pressure buildup has been achieved, capillary forces allow the interface to advance through the feature. In the profile view, the low capillary number causes the interface to take on a spherical arc shape; this shape deforms into a stretched conformation due to the viscous forces that drive the interface into the feature. Once the upper contact line moves into the feature cavity, capillary forces take over once again, causing the interface to rapidly reconfigure into its original equilibrium form. Thus, all aspects of this study are heavily related to the relationship between capillary and viscous forces.

There are several paths that may be taken in pursuing a theoretical and computational understanding of the fluid issues involved in the SFIL process. Now that a more detailed understanding of the mechanism for individual feature filling has been established, future studies can focus on complex feature patterns that are more realistic

94

for circuit designs. This study assumed that the process takes place in a gas that is soluble in the monomer, but it may be more useful for other reasons to use monomers that do not dissolve the surrounding gas. In this case, it would be worthwhile to study gas trapping and the effects it could have on template filling and deformation.

5.4a. Feature Topography

There are many useful problems to consider regarding topography of features on the template. Complex, dense feature patterns are more realistic for microelectronic processing, and these patterns must be filled perfectly in order to obtain a working circuit. There are several possible method for pursuing this study. One is to use the lubrication model developed in this study to model the interface motion through each feature in the pattern; this would be an extremely computationally intensive method and not necessarily useful in obtaining a general understanding of the flow effects due to the topography. A better method may be to consider different types of typical patterns that are useful in microelectronic circuitry. For example, line patterns are particularly prevalent in circuits, so it may be more useful to model flow through line patterns of various dimensions to obtain an understanding of how this type of pattern affects fluid flow. A bulk flow model can then be developed that incorporates general fluid motion through the various types of patterns, thus circumventing the need for high resolution computations.

Some studies have been done in simulating lubrication flow under a rough or porous surface, which could be used as parallels for better modeling bulk lubrication flow under the cavity filled surface of the template in SFIL. Flow effects due to roughness orientation have been incorporated into a flow factor tensor on the Reynolds equation that

captures the effects of the roughness [1,2]. A line pattern on the template might have similar effects on the bulk flow as surface roughness with a given orientation. The effects of elastic deformation due to surface roughness have also been studied [3], which could translate to use in the SFIL problem by comparing the amplitudes of the surface roughness studied to the aspect ratios of the features seen in the SFIL template. Scale-up of permeability models for flow through porous media has long been used to take detailed information about flow through reservoirs and use it in a bulk flow model that uses the detailed flow information to describe the bulk flow [4,5]. This method clearly translates to the need in SFIL modeling to capture detailed flow patterns over the many areas of feature patterns and put those together to simulate the bulk flow under the entirety of the template.

It may also be useful to consider fluid flow along lines and fill effects for patterns that are much smaller than the drop size. Developing a detailed understanding of the lateral motion of the drop interface would be useful in obtaining better strategies of initial drop dispense. Whether it is better for drops to be positioned directly under long lines or small patterns or whether these patterns fill quickly enough via interface movement from capillary filling is a useful question to answer since drop placement could prove to be a key parameter in this regard.

5.4b. Gas Trapping

In the circumstance that the process is run in a gas that does not dissolve in the monomer, the use of multiple drops could trap gas pockets that become high pressure regions inside the fluid as the imprint progresses. Fidelity of the pattern transfer could be

compromised due to gas trapping in template features as well. It would be useful to understand the dynamics of the gas trapping, in terms of the bubble sizes and pressures, as well as the ways in which gas trapping inside features can be avoided, possibly by initial drop configuration or drop sizes. This could become a computationally expensive model due to the resolution required to model the gas trapping in individual features. It may again be useful to consider a few different types of general feature patterns and drop placement scenarios to more effectively study this phenomenon.

An initial computation that would provide some insight on the role of air trapping would be to use the existing model with yet another modified boundary condition on the pressure. This boundary condition must reflect the pressure buildup inside the trapped air bubble as the plates squeeze the bubble. An initial implementation of this pressure buildup might begin with the ideal gas equation,

$$n_{initial} = \frac{P_{atm}V_0}{RT},$$ (5.1)

where n_{inital} is the initial number of moles trapped in the air bubble (an unknown), P_{atm} is the atmospheric pressure or pressure of the surrounding air, if the chamber is at some pressure other than atmospheric, V_0 is the initial volume of the air bubble, R is the ideal gas constant, and T is the surrounding temperature. As the bubble volume changes, presumably decreasing due to the narrowing gap height, the pressure inside the air bubble also changes:

$$P_{bubble} = \frac{n_{initial}RT}{V(t)},$$ (5.2)

where P_{bubble} is the pressure inside the bubble and $V(t)$ is the bubble volume as a function of time. Using the expression for n_{inital} from Equation (5.1),

$$P_{bubble} = \frac{P_{atm}V_0}{V(t)},$$
(5.3)

so that the expression no longer depends on the unknown number of moles inside the bubble. Since the boundary pressure is the pressure difference between atmospheric and inside the bubble, the modified boundary condition can be written as

$$P\big|_{boundary} = P_{atm}\left(\frac{V_0}{V(t)}-1\right) - \frac{1}{Ca*h(x,y,t)},$$
(5.4)

where the capillary pressure at the interface is simply subtracted from the increased pressure due to the squeezing of the bubble between the plates. This simple model would be effective as a first attempt at including the effects of trapped air bubbles on the fluid flow and provide some insight on how to proceed with more detailed analysis of the air trapping issue.

A further consideration to account for is bubble dissolution rate into the monomer, which is dependant on what gas is used in the surroundings. The vapor pressure of the monomer should be taken into consideration since the surrounding medium might actually be the vapor form of the monomer, in which case gas dissolution would be extremely fast and only large bubbles would have to be accounted for in the model, since small bubbles would readily dissolve.

5.4c. Computational Efficiency

In order to solve these computationally complex problems, a parallel code may be considered that can handle more details of feature patterns and gas trapping. I have

written a significant portion of the existing code in parallel form for multiprocessor implementation, but the algorithms must be improved to incorporate these new fluid issues. The pressure solver library, Aztec 2.1 from Sandia National Laboratories, was chosen for its ability to be implemented for parallel processing, and the pressure solver as well as other portions of the code have been written for parallel processing using basic MPI (Message Passing Interface) [6] for communication between processors. Parallel processing may be a viable method to model the complex feature patterns and the effects of gas trapping without the use of a bulk flow model or general studies on a few given types of feature patterns, leading to a commercially useful code that could generate solutions for imprint times, pressures, deformations, and pattern transfer fidelity for a wide variety of feature patterns and process parameters.

5.5. References

[1] W.L. Li, J. of Tribology – Transactions of the ASME 122 (4) (2000) 869-872

[2] S.W. Lo, J. of Tribology – Transactions of the ASME 114 (4) (1992) 747-754.

[3] A.A. Lubrecht, C.H. Venner, Proc. of the Inst. of Mech. Eng. Part J – J. of Engineering Tribology 213 (J5) (1999) 397-404.

[4] D.C. Li, A.S. Cullick, L.W. Lake, SPE Reservoir Engineering 11 (3) (1996) 149-157.

[5] L.J. Durlofsky, Comput. Geosci. 2 (1998) 73-92.

[6] W. Gropp, Using MPI: portable parallel programming with the message passing interface, Cambridge Mass. 1994

Appendix A - Governing Equations

A.1. Lubrication equations

Using the lubrication approximation to simplify the momentum equations, it can be shown [1] that these equations reduce to:

$$\frac{\partial P}{\partial X} = \mu \frac{\partial^2 U_X}{\partial Z^2},$$ (A.1)

$$\frac{\partial P}{\partial Y} = \mu \frac{\partial^2 U_Y}{\partial Z^2},$$ (A.2)

$$\frac{\partial P}{\partial Z} = 0,$$ (A.3)

for rectangular coordinates, where U_X and U_Y represent the X-direction and Y-direction velocities, respectively. In general:

$$\nabla P = \mu \frac{\partial^2 \mathbf{U}}{\partial Z^2}$$ (A.4)

where $\mathbf{U}$ represents the vector form of the velocity. This differential equation can be solved for no-slip boundary conditions at the substrate and template surfaces:

$$\mathbf{U}(Z = H_0) = 0,$$ (A.5)

$$\mathbf{U}(Z = 0) = 0,$$ (A.6)

$$\Rightarrow \mathbf{U} = \frac{1}{2\mu} \nabla P(Z^2 - HZ),$$ (A.7)

The continuity equation will be useful for finding the pressure field:

$$\nabla \bullet \mathbf{U} + \frac{\partial U_Z}{\partial Z} = 0,$$ (A.8)

where W is the vertical velocity. Integrating over the gap and applying the following

boundary conditions leads to an expression for the pressure field:

$$U_Z(Z=H_0)=V, \tag{A.9}$$

$$U_Z(Z=0)=0, \tag{A.10}$$

$$\Rightarrow \nabla \cdot (H^3 \nabla P) = -12\mu V, \tag{A.11}$$

Since the predominant flow is in the X any Y directions, we can express the velocity as an

averaged velocity over the gap:

$$\langle \mathbf{u} \rangle = \int_0^H \frac{1}{2\mu} \nabla P (Z^2 - HZ), \tag{A.12}$$

$$\Rightarrow \langle \mathbf{u} \rangle = \frac{-H_0^2}{12\mu} \nabla P, \tag{A.13}$$

so that the velocity field can be solved for using the gradient of the pressure field from

Equation (A.11).

A.2. Boundary condition

The pressure at the monomer-air interface can be expressed by the Laplace

equation:

$$P = P_{atm} - \gamma \left(\frac{1}{r} + \frac{1}{R} \right), \tag{A.14}$$

where γ is the surface tension of the fluid, R is the larger radius of curvature, which

would be the curvature of the drop from an origin existing inside the drop, and r is the

curvature of the interface from an origin just outside the drop. For simplicity, it is

assumed that the channel width is much smaller than the diameter of the drop. Since R is

101

on the order of the diameter of the drop, typically on the order of millimeters, it is much

larger than r, which scales like the width of the channel and is on the order of less than a

micron, so that the $1/R$ term is negligible compared to $1/r$. This equation can now be

expressed in terms of the contact angles, θ_1 and θ_2, of the fluid on the channel walls, as

illustrated in Figure A.1:

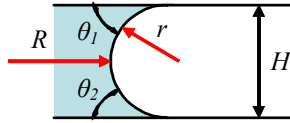$$P = P_{atm} - \gamma \left(\frac{\cos\theta_1 + \cos\theta_2}{H} \right), \tag{A.15}$$

Figure A.1: $R >> r$, where r is the radius of curvature in the profile,
which is a function of the contact angles, θ_1 and θ_2, and gap height H.

For simplicity it may be assumed that the fluid is perfectly wetting on both the

upper and lower plates, so that θ_1 and θ_2 are both 0 and H is the gap height in the channel.

If the monomer is not perfectly wetting, the contact angle would instead be calculated

using the following:

$$\cos\theta = \frac{\gamma_{SG} - \gamma_{SL}}{\gamma_{LG}}, \tag{A.16}$$

The contact angle is thus governed by the surface tension between each phase, where SG

is the solid-gas interface, SL is the solid-liquid interface, and LG is the liquid gas interface.

A.3. References

[1] W.M. Deen, <u>Analysis of Transport Phenomena</u>, Oxford University Press, New York, 1998.

Bibliography

T. Baer, P. R. Schunk, R. A. Cairncross, R. R. Rao, P. A. Sackinger, "A finite element method for free surface flows of incompressible flujids in three dimensions. Part II. Dynamic wetting lines," Int. J. Numer. Meth. Fluids 33 (2000).

T.C. Bailey, S. C. Johnson, S. V. Sreenivasan, J.G. Ekerdt, C.G. Willson, D.J. Resnick, "Step and flash imprint lithography: An efficient nanoscale printing technology", J. Photopolymer Sci. Technol. 15 (3) (2002) 481-486.

T. C. Bailey, S.C. Johnson, M.D. Dickey, J.J. Smith, A.T. Jamieson, E.K. Kim, N.A. Stacey, D. Mancini, W.J. Dauksher, K. Nordquist, D.J. Resnick, S.V. Sreenivasan, J.G. Ekerdt, C.G. Willson, in: Proceedings of the 39th Interface Symposium, 2002.

G. Batch, "Extension of 2 ½D control volume methods for transverse flow at sprues, gates and junctions," International Polymer Processing 12 (1997).

T. D. Blake, J. De Coninck, "The influence of solid-liquid interactions on dynamic wetting," Advances in Colloid and Interface Science 96 (21) (2002).

K.H. Brown, "Economic Challenges on the Path to 22nm", Future Fab International 17 (2004).

R. A. Cairncross, P. R. Schunk, T. Baer, R. R. Rao, P. A. Sackinger, "A finite element method for free surface flows of incompressible flujids in three dimensions. Part I. Boundary fitted mesh motion," Int. J. Numer. Meth. Fluids **33**, 375 (2000)

S.Y. Chou, P.R. Krauss, P.J. Renstrom, "Imprint lithography with 25-nanometer resolution", Science 272 (1996) 85-87.

S.Y. Chou, P.R. Krauss, P.J. Renstrom, "Nanoimprint lithography", J. Vac. Sci. Technol. B. 14 (6) (1996) 4129–4133.

M. Colburn, T. Bailey, B.J. Choi, J.G. Ekerdt, S.V. Sreenivasan, C.G. Willson, "Developments and advantages of step and flash imprint lithography", Solid State Tech. 44 (7) (2001) 67-75.

M. Colburn, B.J. Choi, S.V. Sreenivasan, R.T. Bonnecaze, C.G. Willson, "Ramifications of lubrication theory on imprint lithography", Microelectron. Eng. 75 (3) (2004) 321-329.

M. Colburn, A. Grot, M. Amistoso, B.J. Choi, T. Bailey, J. Ekerdt, S.V. Sreenivasan, J. Hollenhorst, C.G. Willson, "Step and flash imprint lithography for sub-100 nm

patterning", Proc. SPIE 3997 (2000) 453-457.

W.M. Deen, <u>Analysis of Transport Phenomena</u>, Oxford University Press, New York, 1998.

L.J. Durlofsky, "Coarse scale models of two phase flow in heterogeneous reservoirs: volume averaged equations and their relationship to existing upscaling techniques", Comput. Geosci. 2 (1998) 73-92.

H. Fan, Y. Lu, A. Stump, S. T. Reed, T. Baer, P. R. Schunk, V. Luna, G. Lopez, C. J. Brinker, "Rapid prototyping of patterned functional nanostructures," Letters to Nature 405 (56) (2000).

D. Fauchon, H. H. Dannelongue, P. A. Tanguy, "Numerical-simulation of the advancing front in injection molding," International Polymer Processing, **6**, 13 (1991).

W. Gropp, <u>Using MPI: portable parallel programming with the message passing interface</u>, Cambridge Mass. 1994

W.B. Haines, "Studies in the physical properties of soils. IV. A further contribution to the theory of capillary phenomena in soil," J. Agric. Sci. **17,** 264 (1927).

J. Haisma, M. Verheijen, K. Van den Heuvel, J. vandenBerg, "Mold-assisted nanolithography: A process for reliable pattern replication", J. Vac. Sci. Technol. B. 14 (6) (1996) 4124-4129.

B. Heidari, I. Maximov, E. Sarwe, L. Montelius, "Large scale nanolithography using nanoimprint lithography", J. Vac. Sci. Technol. B. 17 (6) (1998) 2961-2964.

C.W. Hirt, B.D. Nichols, "Volume of Fluid (VOF) Method for the Dynamics of Free Boundaries", J. Comp. Phys. 39 (1981) 201–225.

E. Kim, Y.N. Xia, G.M. Whitesides, "Polymer microstructures formed by molding in capillaries", Nature 376 (1995) 581-584.

D.C. Li, A.S. Cullick, L.W. Lake, "Scaleup of reservoir-model relative permeability with a global method", SPE Reservoir Engineering 11 (3) (1996) 149-157.

W.L. Li, "Considerations of roughness orientation and flow rheology", J. of Tribology – Transactions of the ASME 122 (4) (2000) 869-872

S.W. Lo, "On the effects of roughness orientation – a mapping and double scale analysis of flow factors", J. of Tribology – Transactions of the ASME 114 (4) (1992) 747-754.

A.A. Lubrecht, C.H. Venner, "Elastohydrodynamic lubrication of rough surfaces", Proc. of the Inst. of Mech. Eng. Part J – J. of Engineering Tribology 213 (J5) (1999) 397-404.

H. Mavridis, A.N. Hrymak, J. Vlachopoulos, "Transient free-surface flows in injection mold filling," AICHE Journal **34**, 403 (1988).

G.E. Moore, "Cramming more components onto integrated circuits", Electronics 38 (1965) 113-117.

G.E. Moore, "Progress in digital electronics", Proc. IEEE Digital Integrated Electronic Device Meeting (1975) 11-13.

J.D. Plummer, M.D. Deal, P.B. Griffin, <u>Silicon VLSI Technology: Fundamentals, Practice and Modeling</u>, Prentice Hall, Inc. Upper Saddle River NJ, 2000.

S. Reddy and R.T. Bonnecaze, "Dynamics of low capillary number interfaces moving through sharp features", Phys. Fluids 17 (2005) 122104-1 – 122104-6.

S. Reddy, R. T. Bonnecaze, "Simulation of fluid flow in the step and flash imprint lithography process," Microelectron. Eng. 82 (1) (2005) 60-70.

D. J. Resnick, D. Mancinia, W. J. Daukshera, K. Nordquist, T. C. Bailey, S. Johnson, S.V. Sreenivasan, J. G. Ekerdt, C. G. Willson, "Improved step and flash imprint lithography templates for nanofabrication," Microelectron. Eng. 69 (2003) 412-419.

D.J. Resnick, W.J. Dauksher, D.P. Mancini, K.J. Nordquist, T.C. Bailey, S.C. Johnson, N.A. Stacey, J.G. Ekerdt, C.G. Willson, S.V. Sreenivasan, N. Schumaker, "Imprint lithography for integrated circuit fabrication", J. Vac. Sci. Technol. B 21 (6) (2003) 2624-2631.

W.R. Rossen, "Theory of mobilization pressure gradient of flowing foams in porous media .3. Asymmetric lamella shapes", J. Colloid and Interface Science 136 (1) (1990) 38-53.

P. A. Sackinger, P. R. Schunk, R. R. Rao, "A Newton-Raphson pseudo-solid domain mapping technique for free and moving boundary problems: a finite element implementation," J. Comp. Phys. 125 (1996).

H.C. Scheer, H. Schulz, T. Hoffmann, S. Torres, "Problems of the nanoimprinting technique for nanometer scale pattern definition", J. Vac. Sci. Technol. B. 16 (6) (1998) 3917-3921.

S.D. Schuetter, G. A. Dicks, G. F. Nellis, R.L. Engelstad, E.G. Lovell, "Controlling imprint distortions in step and flash imprint lithography", J. Vac. Sci. Technol. B. 22 (6) (2004) 3312-3317.

J.J. Thompson, Naubel Laureate speech, nobelprize.org

E. Ventsel, "Thin Plates and Shells: Theory, Analysis and Applications" New York (2001).

VITA

Shravanthi Reddy was born in Ogden, Utah on January 1, 1979, the daughter of T. Prasanna Reddy and T. Ramakrishna Reddy. She attended The School of St. Helen and St. Katherine in Abingdon, England, earning G.C.S.E. certificates in Latin and English. After finishing her studies at Bonneville High School, Ogden, Utah, in 1997, she entered Princeton University in Princeton, New Jersey, where she played Women's Varsity Tennis and majored in Chemical Engineering. She received the degree of Bachelor of Science in Engineering from Princeton University in May 2001. In September 2001, she entered the Graduate Program in Chemical Engineering at The University of Texas at Austin, where she received a Master of Science in Engineering in December 2005.

She worked as an undergraduate research assistant at The University of Utah in 1998 and 1999 and at Lawrence Berkeley National Laboratories in 2000. She served as a graduate teaching assistant at The University of Texas at Austin for two courses in the Chemical Engineering department, undergraduate Transport and undergraduate Thermodynamics. She also worked as a graduate research intern at Sandia National Laboratories during the Spring and Summer semesters in 2004. Her publications are:

- *"The Dynamics of Low Capillary Interfaces Moving through Sharp Features"*, S. Reddy, R.T. Bonnecaze, **Physics of Fluids** 17 122104, 2005

- *"Simulation of Fluid Flow in the Step and Flash Imprint Lithography Process"*, S. Reddy, R.T. Bonnecaze. **Microelectronic Engineering** 82 (1), 60-70, 2005

- "*Wetting in Pressure Driven Slot Flow*", A. Sun, T.Baer, S. Reddy, L. Mondy, R. Schunk, R. Rao, D. Noble, J. Bielenber, A. Graham, P. Sackinger, **Moving**

Boundaries 2005 , WIT Press, UK

- *"Simulation of Fluid Flow in the Step and Flash Imprint Lithography Process"*, S. Reddy, R.T. Bonnecaze, **Proceedings of the SPIE** 5751 200-209, 2005

- *"Fluid Dynamics in the Nano-imprint process of Step and Flash Imprint Lithography"* S. Reddy (speaker), R.T. Bonnecaze, **International Nanoimprint and Nanoprint Technology Conference**, Vienna Austria, 2004

Permanent Address: 5974 South Sharon Circle, Ogden, Utah 84403

This dissertation was typed by the author.